

Optimization of composition, structure and mechanical strength of bioactive 3-D glass-ceramic scaffolds for bone substitution

*Original*

Optimization of composition, structure and mechanical strength of bioactive 3-D glass-ceramic scaffolds for bone substitution / Baino, Francesco; Ferraris, Monica; Bretcanu, OANA ANCA; Verne', Enrica; VITALE BROVARONE, Chiara. - In: JOURNAL OF BIOMATERIALS APPLICATIONS. - ISSN 0885-3282. - ELETTRONICO. - 27:(2013), pp. 872-890. [10.1177/0885328211429193]

*Availability:*

This version is available at: 11583/2451175 since:

*Publisher:*

Sage publications

*Published*

DOI:10.1177/0885328211429193

*Terms of use:*

This article is made available under terms and conditions as specified in the corresponding bibliographic description in the repository

*Publisher copyright*

(Article begins on next page)

# Optimization of Composition, Structure and Mechanical Strength of Bioactive 3-D Glass-Ceramic Scaffolds for Bone Substitution

FRANCESCO BAINO,<sup>1</sup> MONICA FERRARIS,<sup>1</sup> OANA BRETCANU,<sup>1,2</sup>

ENRICA VERNÉ<sup>1</sup> AND CHIARA VITALE-BROVARONE<sup>1,\*</sup>

This is the author post-print version of an article published on *Journal of Biomaterials Applications*, Vol. 27, pp. 872-890, 2013 (ISSN 0885-3282).

The final publication is available at

<http://dx.doi.org/10.1177/0885328211429193>

This version does not contain journal formatting and may contain minor changes with respect to the published edition.

The present version is accessible on PORTO, the Open Access Repository of the Politecnico of Torino, in compliance with the publisher's copyright policy.

Copyright owner: *Sage publications*.

<sup>1</sup> *Materials Science and Chemical Engineering Department, Politecnico di Torino, Corso Duca degli Abruzzi 24, 10129 Torino, Italy.*

<sup>2</sup> *School of Mechanical and Systems Engineering, Newcastle University, NE1 7RU, United Kingdom.*

\* Corresponding author: Chiara Vitale-Brovarone

E-mail: [chiara.vitale@polito.it](mailto:chiara.vitale@polito.it)

Tel.: +39 011 090 4716

Fax: + 39 011 090 4699

**ABSTRACT:** Fabrication of 3-D highly porous, bioactive and mechanically competent scaffolds represents a significant challenge of bone tissue engineering. In this work, Bioglass<sup>®</sup>-derived glass-ceramic scaffolds actually fulfilling this complex set of requirements were successfully produced through sponge replication method. Scaffold processing parameters and sintering treatment were carefully designed in order to obtain final porous bodies with pore content (porosity above 70%vol.), trabecular architecture and mechanical properties (compressive strength up to 3 MPa) analogous to those of cancellous bone. Influence of Bioglass<sup>®</sup> particles size on the structural and mechanical features of the sintered scaffolds was considered and discussed. Relationship between porosity and mechanical strength was investigated and modelled. 3-D architecture, porosity, mechanical strength and *in vitro* bioactivity of the optimized Bioglass<sup>®</sup>-derived scaffolds were also compared to those of CEL2-based glass-ceramic scaffolds (CEL2 is an experimental bioactive glass originally developed by the authors at Politecnico di Torino) fabricated by the same processing technique, in an attempt at understanding the role of different bioactive glass composition on the major features of scaffolds prepared by the same method.

**KEY WORDS:** Glass; Sponge replication; Mechanical strength; Bioactivity; Bone tissue engineering.

## INTRODUCTION

**Over the last** 40 years, bioceramics have attracted increasing interest as implantable materials in the field of orthopaedic surgery and bone reconstruction [1-4]. In the mid 1980s, the osteoconductive properties of calcium phosphates (CaPs), including primarily hydroxyapatite (HA) and  $\beta$ -tricalcium phosphate ( $\beta$ -TCP), led to their use as a promising alternative to autograft and allograft for bone tissue repair [5]. Most of synthetic bone substitutes in current use are porous blocks of biphasic HA/ $\beta$ -TCP composites [6]. The overall degradation rate of the material can be controlled by acting on the amount of  $\beta$ -TCP, which has a fast *in vivo* resorption rate as compared to HA, thereby leading to custom-made implant (slower resorption for patients with slower bone regeneration). However, the commercially available CaP implants are generally characterized by high brittleness associated to low crack resistance [7], which often makes them difficult to handle during surgery and therefore restricts their use to non-load bearing applications; furthermore CaPs, although being similar to bone mineral from chemical and crystallographic viewpoints, are not properly bioactive and do not stimulate bone cells towards osteogenesis [1,4].

As extensively emphasized by several authors, bioactive glasses have a great potential for overcoming the limitations of CaPs as they exhibit higher mechanical properties and are able to bond to bone creating a stable interface [1-4,8-10]. Their bioactivity is due to the formation of a HA or apatite-like layer on their surface after contact with body fluids [1]. The first bioactive glass, called Bioglass<sup>®</sup>, was synthesized and investigated by Hench and co-workers in the early 1970s [11]; since then, several glasses and glass-ceramics of various compositions have been proposed as bone graft biomaterials [12].

Bioglass<sup>®</sup> has been marketed worldwide since 1985 as a fine particulate for dental application (Perioglas, NovaBone, USA) and since the mid 1990s in form of dense blocks and granulates of various size for bone defect filling in orthopaedics and dentistry. It has been also demonstrated that Bioglass<sup>®</sup> promotes stem cells differentiation into osteoblasts and that its ionic dissolution products

have a direct effect in stimulating bone cells genes towards a path of regeneration and self-repair [13-15].

To the best of the authors' knowledge, however, the use of porous Bioglass<sup>®</sup> in the surgical practice has not yet been introduced. In fact, the development of 3-D Bioglass<sup>®</sup> scaffolds for clinical use is currently in progress: although Bioglass<sup>®</sup> was demonstrated to be an excellent bioactive material for promoting bone tissue regeneration, all porous bodies produced from it exhibited relevant brittleness and poor mechanical strength. In 2006, Chen et al. [16] pioneered the fabrication of glass-ceramic (GC) Bioglass<sup>®</sup>-derived scaffolds by sponge replication technique: the scaffolds had porous content (> 85 %vol.) and 3-D architecture that closely mimicked those of cancellous bone, but their mechanical strength (0.3-0.4 MPa) was almost one order of magnitude lower than that of spongy bone (2-12 MPa [1]). One year later, Bretcanu et al. [17] fabricated porous composites by coating foam-like GC-Bioglass<sup>®</sup> scaffolds with poly(3-hydroxybutyrate): the polymer strengthened the inorganic porous matrix acting as a glue and holding the glass-ceramic particles together when the scaffold struts begun to fail. The compressive strength of these porous composites (up to 1.5 MPa) was twice that of bare GC-Bioglass<sup>®</sup> scaffolds (0.3-0.4 MPa [16]), but these results are still unsatisfactory for clinical use. In 2009, Wu et al. [18] manufactured GC-Bioglass<sup>®</sup> scaffolds by using rice husk as a volatile pore former: the mechanical strength of these scaffolds ranged within 5.4-7.2 MPa and, therefore, was comparable to that of spongy bone, but their porosity content (~45 %vol.) was below the lower threshold required for porous bone grafts (50-70%vol. [19]). Furthermore, these scaffolds exhibited a 3-D porous architecture far from that of spongy bone, with poorly interconnected elongated pores resembling the shape and size of the sacrificial rice husks.

Very recently, Bellucci et al. [20] produced GC-Bioglass<sup>®</sup> scaffolds by combining sponge replication with polyethylene burning-out method, but no data about their mechanical properties have been reported yet.

It is evident that the achievement of a satisfactory compromise between pores content and adequate mechanical strength is a crucial issue in scaffolds manufacturing. Recently, Vitale-Brovarone et al.

[21] proposed an effective processing schedule to fabricate bioactive glass-ceramic scaffolds with promising properties (porosity > 50% vol., compressive strength > 5 MPa) using CEL2 glass powder (a glass composition developed at Politecnico di Torino) [22]. This method for scaffolding was adopted in the present work to fabricate Bioglass<sup>®</sup>-derived scaffolds able to be highly-porous, mechanically-competent and bioactive at the same time. Furthermore, a comparison between architectural/mechanical features and bioactive behaviour of the so-obtained Bioglass<sup>®</sup> - and CEL2-derived scaffolds is presented and discussed, in the attempt at understanding the role of different bioactive glass composition on the major features of scaffolds prepared by the same method.

## **MATERIALS AND METHODS**

### **Starting glasses synthesis**

Two silicate glasses, Bioglass<sup>®</sup> and CEL2, were used as starting materials for scaffolds fabrication; their molar compositions are listed in Table 1. Bioglass<sup>®</sup> is a biomaterial well known for many years in the biomedical field [8]; CEL2 is a silicate glass that has been originally developed and studied by Vitale-Brovarone and co-workers at Politecnico di Torino since the mid 2000s [22,23]. Both glasses were synthesized by melting high-purity raw products (Sigma-Aldrich) in a platinum crucible in air (Table 2); the melt was then quenched into cold water to obtain a “frit” that was ground by zirconia ball milling. Glass powders were eventually sieved to obtain particles with grain size below 32 µm to be used for fabricating the scaffolds.

Furthermore, commercial Bioglass<sup>®</sup> powder (NovaBone, USA) with particle size below 5 µm were also used for making separate scaffold batches.

From now on, the two types of Bioglass<sup>®</sup> powders will be distinguished as follows: the melt-derived Bioglass<sup>®</sup> sieved below 32 µm will be referred to as BG32, whereas the commercial one will be denoted as BG5.

## Glasses characterization

As-poured glasses underwent wide-angle ( $2\theta$  within  $10\text{-}70^\circ$ ) X-ray diffraction analysis (WA-XRD) using a X'Pert diffractometer operating at 40 kV and 30 mA (Bragg-Brentano camera geometry with Cu  $K\alpha$  incident radiation, incident wavelength  $\lambda = 1.5405 \text{ \AA}$ , step size  $\Delta(2\theta) = 0.02^\circ$ , fixed counting time of 1 s per step).

Glass powders were silver-coated and their morphology was investigated by scanning electron microscopy (SEM, Philips 525 M; accelerating voltage = 15 kV).

The sintering process of glass powder compacts was monitored by hot-stage microscopy (HSM) (Expert System Solutions instrument) performed in air atmosphere to approximate the chemo-environmental conditions of the furnace chamber during the scaffold heat treatment. This analysis provides useful information for selecting the appropriate sintering temperature in order to obtain, at least ideally, scaffolds with well-densified trabeculae, high mechanical strength and adequate porous content for bone tissue engineering applications. HSM allows the quantification of the shrinkage due to sintering by measuring the variation of specimen size during a controlled heating process (heating rate:  $20 \text{ }^\circ\text{C}\cdot\text{min}^{-1}$ ). The samples for HSM analysis were prepared by manually pressing the glass powders using a small cylindrical mould (base diameter  $\sim 1 \text{ mm}$ , height  $\sim 3 \text{ mm}$ ). Sample shrinkage at different temperatures,  $S_{\text{glass},T} (\%)$ , was assumed as isotropic and was estimated as:

$$S_{\text{glass},T} = \left(1 - \frac{A_T}{A_0}\right) \times 100 \quad (1)$$

where  $A_0$  is the area of the sample at room temperature and  $A_T$  is the sample area at the temperature  $T$  ( $^\circ\text{C}$ ).

Differential thermal analysis (DTA) of glass powders was carried out by using a DTA7 Perkin-Elmer instrument (temperature range:  $50\text{-}1300 \text{ }^\circ\text{C}$ ; heating rate:  $20 \text{ }^\circ\text{C}\cdot\text{min}^{-1}$ ). Pure alumina powder

(Sigma-Aldrich) was used as a reference material and for baseline determination. The characteristic temperatures of glasses, i.e. glass transition temperature ( $T_g$ ), onset crystallization temperature ( $T_x$ ), peak crystallization temperature ( $T_c$ ), were assessed directly from the DTA plots. Melting temperature ( $T_m$ ) of glasses was assessed by comparing HSM and DTA results (both analyses were performed according to analogous experimental conditions). It is worth anticipating that, when  $T_m$  is reached, the materials will be no longer the original glasses only, but glass-crystals composites (glass-ceramics) due to the nucleation of crystalline phases upon heating. Therefore, the use of expressions like “liquid point/liquid temperature of the material” instead of “glass melting temperature” would be more appropriate. However, in the present work we will follow the common practice adopted in the scientific literature, which involves the use of the latter locution for sake of simplicity.

### **Scaffolds fabrication**

Sponge replication was chosen for scaffolding because it is an easy, low-cost and efficient method to obtain scaffolds with trabecular architecture closely mimicking that of cancellous bone [12,16]. Commercial polyurethane (PU) porous templates were coated with glass powder by impregnating polymer cubic blocks ( $15.0 \times 15.0 \times 15.0 \text{ mm}^3$ ) in a water-based glass slurry (weight composition: 30% glass, 64% distilled water, 6% poly(vinyl alcohol) (PVA)) [21]. After PVA hydrolysis under continuous stirring at 80 °C, the glass powder was dispersed in the solution and stirred for 0.5 h; the water eventually evaporated during PVA dissolution was re-added to the slurry. The sponge blocks were soaked into the glass slurry for 60 s, extracted and compressed (20 kPa for 1 s) up to 60% in thickness along the three spatial directions in order to homogeneously remove the exceeding slurry. This infiltration/compression cycle was repeated for three times; after that, a final cycle of impregnation alone without compression was performed. The samples were dried at room temperature for 6 h and thermally treated in order to remove the organic phase and to sinter the



inorganic one, thereby obtaining macroporous glass-derived scaffolds. CEL2-derived scaffolds were all sintered at 1000 °C for 3 h; as regards Bioglass<sup>®</sup>-derived scaffolds, the sintering time was always set at 3 h, but different sintering temperatures were experimented. For sake of clearness, the scaffolds batches sintered at different temperatures will be labelled by means of the acronym BG $n$ - $T$ , where  $n = 32$  or 5 ( $\mu\text{m}$ ) is the glass particle size and  $T$  (°C) is the sintering temperature.

### Scaffolds characterization

The scaffolds ground in powders underwent WA-XRD investigation (see the section “Glasses characterization” before) to assess the presence of crystalline phases nucleated during the thermal treatment of sintering. Phase identification was performed by using X’Pert HighScore program equipped with PCPDFWIN database.

The scaffolds were silver-coated and analyzed from a morphological viewpoint by SEM (see the section “Glasses characterization” before) to assess pores/struts size and shape.

The volumetric shrinkage  $S_{scaffold}$  (%), due to the polymeric template removal and to the glass softening-sintering, was calculated as

$$S_{scaffold} = \left( 1 - \frac{V_s}{V_0} \right) \times 100 \quad (2)$$

where  $V_0$  is the volume of the glass-impregnated sponge before sintering and  $V_s$  is the volume of the final scaffold.

The porosity content  $P$  (%vol.) was calculated by means of geometrical weight-volume measurements as

$$P = \left( 1 - \frac{\rho_s}{\rho_b} \right) \times 100 \quad (3)$$

where  $\rho_b$  is the density of bulk material and  $\rho_s$  is the apparent density of the scaffold (weight/volume ratio).

Quantitative assessment of pores size distribution was carried out by image analysis (ImageJ software) on low-magnification SEM pictures of polished cross-sections of the scaffolds.

Scaffolds compressive strength was evaluated by means of crushing tests (MTS System Corp. apparatus, cross-head speed = 1 mm·min<sup>-1</sup>); the failure stress  $\sigma_c$  (MPa) was obtained as

$$\sigma_c = \frac{L_M}{A_R} \quad (4)$$

where  $L_M$  (N) is the maximum compressive load registered during the test and  $A_R$  (mm<sup>2</sup>) is the resistant area perpendicular to the load axis.

*In vitro* tests were performed to assess scaffolds bioactivity by soaking the samples for 7 days in acellular simulated body fluid (SBF), prepared according to the protocol proposed by Kokubo and Takadama [24]; a large part of the scientific community has recognized this assay as a valuable method for preliminary assessment of biomaterials bioactivity. Specifically, the scaffolds were soaked for different time frames in 30 ml of preheated SBF maintained at 37 °C in an incubator (Bicasa). Every 48 h the samples were extracted from the solution, gently washed with distilled water and soaked in preheated fresh SBF. At the end of the experiment, the samples were gently washed with distilled water, dried at room temperature, silver-coated and investigated by SEM and energy dispersive spectroscopy (EDS; Philips Edax 9100) for compositional analysis.

## RESULTS AND DISCUSSION

### Starting glasses

#### *Glass powders morphology*

Commercial Bioglass<sup>®</sup> powders (BG5) are shown in Figure 1(a); BG5 particles are irregular with sharp edges and, being very fine (< 5 µm), showed the tendency to agglomerate forming aggregates.

Glass with the same composition of Bioglass<sup>®</sup> was also produced in our laboratories through a melting route; the final sieved glass particles (BG32) used for scaffolding are shown in Figure 1(b). An analogous processing schedule was adopted to produce CEL2 powders (Figure 1(c)). The morphology of BG32 and CEL2 particles was non-spherical, irregular and angular; a bimodal distribution of glass particles size can be qualitatively observed, since most of them were within 5-20  $\mu\text{m}$  and relatively few particles were detected in the 20-32  $\mu\text{m}$  range.

### *Thermal analyses*

BG32, BG5 and CEL2 powders underwent HSM and DTA investigations, whose results are reported in Figures 2-7. The characteristic temperatures of the glasses, assessed by DTA, are also reported in Table 3. It is interesting to notice that particle size influences the position of the characteristic temperatures of Bioglass<sup>®</sup>. In fact, the characteristic temperatures of BG32 exhibit a slight shift towards higher values in comparison to BG5. This finding is in accordance to the results recently reported by Erol et al. [25], who demonstrated that, for the same glass, crystallization temperature ( $T_x$  and  $T_c$ ) increase with the increase in particle size.

The reduction of samples dimensions (densification) during the sintering process can be clearly observed by looking at Figure 2, Figure 4 and Figure 6. The specimens seem to maintain their cylindrical shape, that originates rectangular silhouettes, up to  $\sim 1150^\circ\text{C}$ ,  $\sim 1100^\circ\text{C}$  and  $\sim 950^\circ\text{C}$  for BG32, BG5 and CEL2, respectively. It is interesting to observe that CEL2 sample undergoes significant shrinkage in the 500-700  $^\circ\text{C}$  range (Figure 6 and Figure 7(a)). If temperature further increases, the glasses become softer and viscosity decreases, leading to distortion and final melting of the sample.

A quantitative evaluation of the variations of glasses shrinkage depending on the sintering temperature can be derived from the curves plotted in Figure 3(a), Figure 5(a) and Figure 7(a). As clearly evident from the HSM curves reported in Figure 3(a) and Figure 5(a), the thermal behaviour of BG32 and BG5 powders is different. BG32 powder compact exhibits no evident densification

steps and seems to keep its unchanged shape up to  $T_1 \approx 1150$  °C (Figure 2), when the material begins to melt. Increasing the temperature above  $T_1$ , the material becomes softer and the viscosity significantly decreases, thereby leading to a prompt reduction of the sample silhouette (Figure 3), which corresponds to the melting of the glass. BG32 seems to exhibit no significant stage of densification before melting (Figure 3(a)): in fact, it was estimated that  $S_{BG32,1150} \approx 2$  %.

On the contrary, as clearly evident in Figure 5(a), BG5 exhibits a 2-step densification behaviour. This observation is consistent with the findings reported by Bretcanu et al. [26]. The first step of densification ( $\Delta S_1$ ) occurs between  $T_1 \approx 550$  °C and  $T_2 \approx 615$  °C: it begins shortly after the  $T_g$  is reached (Table 3), i.e. when viscous flow sintering starts. From a quantitative viewpoint, we estimated  $S_{BG5,615} \approx 6$  % . As shown in Figure 5, crystallization of BG5 particles begins before  $T_2$  and occurs up to  $\sim 750$  °C; hence, the material will be highly crystalline before the second stage of densification ( $\Delta S_2$ ) takes place above  $T_3 \approx 900$  °C, as also demonstrated by other authors [26,27].

From a theoretical viewpoint, the whole plateau ( $T_3 - T_2$ ), observed between the two stages of shrinkage in Figure 5(a), should correspond to the crystallization process, during which the viscosity increases and viscous flow sintering is inhibited. If temperature increases again, viscosity decreases and the second stage of shrinkage occurs. Estimating  $T_4 \approx 1100$  °C as the end temperature of the second stage of BG5 densification or, alternatively, as the onset temperature of BG5 melting, we calculated  $\Delta S_2 \approx 20$  %; therefore, the total shrinkage of BG5 up to  $T_4$  was  $S_{BG5,1100} \approx 26$  %.

Finally, Figure 7(a) reveals that CEL2 exhibited a 1-step densification behaviour ( $\Delta S_{tot}$ ); specifically, densification begins at  $T_1 \approx T_g$  (beginning of viscous flow sintering) and is fully completed when crystallization starts ( $T_2 \approx T_{x1}$ ). We estimated that the shrinkage up to  $T_2$  was  $\Delta S_{tot} = S_{BG5,650} \approx 25$  %. CEL2 specimen started to expand at  $T_3 \approx 925$  °C, and the melting onset occurred at  $T_4 \approx 1000$  °C.

Relevant expansion of CEL2 above  $T_3$  (Figure 6 and Figure 7(a)) might be related to the crystallization of the second phase  $\text{Ca}_2\text{Mg}(\text{Si}_2\text{O}_7)$  [21] (see also the section “Structural analysis” later), considering that full densification was already achieved. This behaviour was not observed in Bioglass<sup>®</sup>, as its expansion at high temperature due to crystallization is balanced by shrinkage. This issue was discussed in an interesting work by Huang et al. [27], who investigated the behaviour of commercial Bioglass<sup>®</sup> powders – i.e. the BG5 used in the present work – upon heating: up to 900 °C, sintering is fully suppressed by crystallization, but, if temperature is further increased, shrinkage and densification can significantly occur. These findings are in good agreement with the results reported in the present work.

#### *Sintering and crystallization of the glasses: quantitative considerations*

Glass stability against crystallization upon heating can be evaluated, from a quantitative viewpoint, by considering the difference  $T_x - T_g$  estimated from DTA plots (Table 3). This parameter indicates the tendency towards crystallization of the glass composition, as a greater difference reveals a lower tendency to crystallization, i.e. a greater stability of the materials in its glassy state upon heating.

Hruby [28] proposed another parameter,  $K_H$ , defined as

$$K_H = \frac{T_x - T_g}{T_m - T_x} \quad (5)$$

that can be used to measure glass stability. According to Hruby, the larger  $K_H$  of a certain glass, the greater its stability against crystallization upon heating. Therefore, as shown in Table 3, Bioglass<sup>®</sup> revealed a higher crystallization ability in comparison to CEL2 and, therefore, a lower stability in glass form.

It is well known that viscous flow sintering of glass particles can effectively occur when their surface tension is high and the viscosity is low, i.e. when the glass shows its lower viscosity, without, ideally, any crystallization process in action [29,30]. Recently, Lara et al. [31] introduced a new parameter,  $S_c$  (sinterability), that estimates the competition between glass sintering and

crystallization of glass powders during heating. It is defined as  $S_c = T_x - T_{MS}$ , where  $T_{MS}$  is the temperature of maximum shrinkage determined from HSM. As explained by Lara et al. [31], the difference between starting crystallization and maximum shrinkage temperatures is a measure of the ability of sintering versus crystallization: the greater  $S_c$ , the more independent are the kinetics of the two processes.

Furthermore, we propose a general rule for the interpretation of  $S_c$ : if  $S_c < 0$ , only partial densification is achieved before crystallization begins; otherwise, if  $S_c \geq 0$ , full densification occurs prior to crystallization. Therefore, higher  $S_c$  are related to higher final densities, which indicated a better sintering behaviour involving a higher densification of the final sample.

In the present work, it is worth carefully considering the meaning of  $S_c$  for each glass. As regards BG32, the glass powder compact undergoes no shrinkage up to  $T_1 \approx 1150$  °C, when the material begins to melt (Figure 2 and Figure 3); therefore, we can assume as a limit  $T_{MS} = T_1$ , and, accordingly, we have  $S_c < 0$ . A similar situation can be observed for BG5: crystallization of the glass occurs prior to significant densification, as the major step of shrinkage ( $\Delta S_2$ ) takes place above 900 °C. By looking at Figure 5, we can assume as a limit  $T_{MS} = T_4$ : hence, also for BG5 we have  $S_c < 0$ .

The situation is different for CEL2, as crystallization begins when the maximum shrinkage is reached. From Figure 7(a) we can assume that  $T_{MS} = T_2 \approx T_x$ : hence, we have  $S_c \approx 0$ . Therefore, CEL2 exhibits a higher sinterability than Bioglass<sup>®</sup>, which eventually will ensue in a better densification of the material.

#### *Remarks on the selection of the sintering temperature from thermal analysis data*

Data from thermal analyses are very useful to guide researchers in selecting the “optimal” sintering temperature for fabricating scaffolds, in order to obtain a good compromise between densification, required to strengthen the struts of the final porous body, and pore content, which should be above

50 % vol. to promote cell colonization, implant vascularisation and bone in-growth [19]. However, it should be underlined that the sintering process of scaffolds obtained by sponge replication, like those fabricated in this work, is quite different from the sintering of compacts of glass powders, like those used for HSM. First, glass-impregnated PU sponges exhibit large macropores due to the 3-D architecture of the polymer template, whereas the pores detectable in compacts of glass powders are attributable to small intra-particulate voids. Furthermore, during thermal treatment of the glass-coated polymer we assist not only to densification/crystallization of glass particles, but also to the burning-out of the polymer template, which may eventually ensue in significant additional contraction of the structure on its own weight. From a theoretical viewpoint, HSM of a glass-impregnated sponge would give more precise information to select the optimal sintering temperature for scaffolding, but such a test is not feasible due to obvious working difficulties such as cutting and impregnation of very small sponge pieces suitable to be introduced in the HSM equipment.

In the authors' view, HSM on glass powder compacts is therefore useful to understand glass behaviour upon heating and can provide a range of potentially suitable temperatures for sintering sponge-replicated scaffolds, but the actually "optimal" sintering temperature can be found only through a fine evaluation involving the factual fabrication of test specimens, as we did in the present work. As a preliminary and general criterion, if a wholly glass material is desired after thermal treatment, sintering temperature(s) should be chosen in the range between the maximum densification and the onset of crystallization. However, if glass-ceramic structures are required – for instance, for high-strength applications as in the case of biomedical scaffolds – or if crystallization occurs before densification is completed (in this sense, the behaviour of BG5, reported in Figure 5, is emblematic), temperatures between maximum shrinkage and melting onset are usually considered.

## **Glass-derived scaffolds**

The processing schedule developed by the authors for fabricating GC-CEL2 scaffolds [21] was adopted in this work to manufacture Bioglass<sup>®</sup>-derived scaffolds. The features of the commercial open-cell PU sponge used as a sacrificial template were described elsewhere [21].

### *Structural analysis*

As-melt BG32 is a completely amorphous material: only a broad halo and no diffraction peaks are visible in the corresponding XRD pattern (Figure 8). XRD plots of GC-BG32 scaffolds sintered at different temperatures and ground in powder for diffraction analysis are also reported in Figure 8. The main crystalline phase was identified as  $\text{Na}_2\text{CaSi}_2\text{O}_6$ , as already reported by other authors [32-34]. A secondary phase corresponding to  $\text{Na}_2\text{Ca}_4(\text{PO}_4)_2\text{SiO}_4$  was also identified, as expected from the literature [26,33,34]; this phase was not always detected and reported in the literature due to the difficult interpretation of XRD data.

For sake of discussion, it is worth mentioning that there is no unanimity in the literature about the identification of the major phase of GC-Bioglass<sup>®</sup>. Over the years, different research groups suggested two possible options (both of them are sodium-calcium silicates):  $\text{Na}_2\text{Ca}_2\text{Si}_3\text{O}_9$  [16,18,26] and  $\text{Na}_2\text{CaSi}_2\text{O}_6$  [32-34]. Recently, Bellucci et al. [35] hypothesized a coexistence between the two phases. In the present work, we confirm that the phase assignment already suggested by Lin et al. [32] and Lefebvre et al. [33,34] is the most likely.

XRD pattern of GC-CEL2 is not reported, as the identification of the crystalline phases ( $\text{Na}_4\text{Ca}_4(\text{Si}_6\text{O}_{18})$  and  $\text{Ca}_2\text{Mg}(\text{Si}_2\text{O}_7)$ ) was discussed elsewhere in detail [21].

### *Architecture and morphology*

First, non-commercial BG32 powders were used as a starting material in the sponge replication process. Different sintering temperatures were adopted, ranging from 1000 to 1180 °C; sintering temperatures higher than 1180 °C led to scaffold collapse. A comparison of the different sintering



results is shown in Figure 9. After sintering, a glass-ceramic replica of the starting polymer template, closely mimicking the trabecular architecture of natural cancellous bone with most of pores in the 100-600  $\mu\text{m}$  range, is successfully achieved in all cases. However, it cannot be ignored that unsatisfactory sintering results were obtained at treatment temperatures up to 1150  $^{\circ}\text{C}$  (Figures 9(a)-(d)). In fact, sponge architecture was faithfully replicated, but scaffold trabeculae are not sufficiently densified and the original glass particles with sharp edges can still be observed. These scaffolds were characterized by a noticeable brittleness, were susceptible of damage when handled and, therefore, were mechanically unsuitable for possible clinical use. In Figure 9(d) a hollow central region in scaffold struts (white circle), corresponding to the trace of the PU template removed by thermal treatment, is clearly distinguishable. Chen et al. in 2006 [16] and Bretcanu et al. in 2007 [17] also reported this unwanted feature as peculiar for Bioglass<sup>®</sup>-derived glass-ceramic scaffolds. By increasing the temperature above 1150  $^{\circ}\text{C}$ , viscosity decreases and viscous flow sintering is enhanced. Scaffold trabeculae progressively densify, thereby eventually leading to a typical round-shaped and relatively smooth texture of the strut (Figures 9(h),(i)), on the surface of which the sharp and well-defined original glass particles are no longer distinguishable. It is interesting to notice that GC-BG32-1180 scaffolds maintained their cubic form without distortion (Figure 9(g)), despite the significant volume shrinkage of the macrostructure ( $> 60\%$ , as reported in Table 4). This finding is very important in view of the possible clinical use of the scaffold, if bone substitutes of complex shape are needed for specific bone regeneration applications.

The same processing method used to produce GC-BG32 scaffolds was also adopted to manufacture GC-BG5 scaffolds (Figure 10). On the basis of the shrinkage observed in the HSM (Figure 4 and Figure 5(a)), the sintering temperature was first set at 1100  $^{\circ}\text{C}$ , which corresponds to the onset of BG5 powders melting ( $T_4$  of Figure 5(a)). After sintering, a glass-ceramic replica of the polymer template was obtained: scaffold struts appeared to be well-densified (Figure 10(b)) and, from a qualitative viewpoint, the scaffold was mechanically competent and could be handled without undergoing any damage. No evidence of template-derived cavities inside the struts were detected

(see the white circles in Figure 10(a)). Thermal treatment at temperature higher than 1100 °C caused scaffold collapse: due to temperature increase, glass viscosity decreases and the scaffold porous structure readily deforms under its own weight.

The architectural features of GC-CEL2 scaffolds were extensively presented and discussed elsewhere [21]; for sake of completeness, a polished cross-section and a detail of pore network are shown in Figure 11 .

It is worth underlining that the most promising scaffolds, i.e. the best densified ones, all exhibit an adequate pore content (> 50% vol. [19]) for bone regeneration applications, as reported in Table 4. The trabecular network of interconnected macropores (size within 100-600 µm) is expected to allow cell colonization and migration in the whole scaffold structure (including its inner region), bone tissue in-growth and *in vivo* blood vessel access.

Furthermore, pores size distribution was investigated by means of image analysis (ImageJ program) performed on polished cross-sections of the scaffolds acquired by SEM. The pores were approximated as circular by the software; hence, the equivalent pore diameter  $D_{eq}$  (µm) was calculated as  $D_{eq} = 2\sqrt{A_p/\pi}$ , where  $A_p$  (µm<sup>2</sup>) is the pore area measured by the program. An example of pores size distribution of the most significant scaffolds batches is reported in Figure 12; only large macropores (50-1000 µm) were considered for better readability of the bar chart. It should be carefully taken into account that cells play a key role in implanted porous biomaterials; in the light of this consideration, the importance of pores at the upper macro-scale is really crucial to promote the effective osteointegration of the scaffold. As underlined in the literature [12,19], interconnected porosity above 10 µm is generally useful for cells penetration; more specifically, pores ranging within 100-600 µm allow bone in-growth and blood vessel access, and pores above 600 µm can also lower the Young's modulus of the implant thereby reducing the stress-shielding phenomenon and provide facilities for scaffold fixation to host bone by surgical wires. As shown in Figure 12, for all the three scaffolds batches ~50% or more of pores ranged within 100-1000 µm and, furthermore, were related to above 90% of the total pores area; accordingly, these macropores

are large enough to potentially allow bone in-growth and vascularisation after *in vivo* implantation of the scaffolds.

### *Mechanical strength*

Table 4 collects the results of compressive tests performed on the most significant scaffolds batches produced in this work. As regards GC-BG32 scaffolds, it is interesting to observe that an increment of sintering temperature from 1100 to 1180 °C involves an increase of mechanical strength by a factor ~6.5. This can be essentially attributed to two reasons: (i) sintering at higher temperature is accompanied to a higher volumetric shrinkage of the scaffold, involving a lower pore content in the final porous body; (ii) by adopting a higher sintering temperature, an enhanced densification of scaffold trabeculae is achieved, as can be immediately observed by comparing Figure 9(c) (GC-BG32-1100 scaffold) with Figure 9(i) (GC-BG32-1180 scaffold).

Sintering of Bioglass<sup>®</sup>-derived (starting powders < 5 µm) glass-ceramic scaffolds at 1100 °C was already reported by Bretcanu et al. [17], who obtained a compressive strength of ~0.2 MPa: this value is more than ten times lower than that reported in the present work (2.5 MPa). This remarkable discrepancy can be explained considering that the method of PU sponge impregnation is different (one cycle of impregnation for the scaffolds prepared by Bretcanu et al. [17] vs. four cycles adopted in the present work), as well as the sintering time (1 h vs. 3 h). Optimization of scaffold impregnation process and sintering treatment have now led to better densified struts, which ensues in a strengthened scaffold structure. Furthermore, it cannot be ignored that the scaffolds produced by Bretcanu et al. [17] exhibited a hollow central region in their struts, whereas no evidence of this tricky feature was noticed in the GC-BG-1100 scaffolds prepared in this work (Figure 10(b)).

It is also interesting to compare the properties of GC-BG32-1180 and GC-BG5-1100 scaffolds: as reported in Table 4, both exhibit analogous volumetric shrinkage and pore content, but the compressive strength of GC-BG5-1100 scaffolds is twofold than that of GC-BG32-1180 ones. This

can be attributable to a better coating of PU template and a higher homogeneity obtained by the very fine commercial Bioglass<sup>®</sup> particles (< 5  $\mu\text{m}$ ) in comparison to non-commercial ones (< 32  $\mu\text{m}$ ). It is worth further remarking that BG32 particles undergo very slight densification upon heating (Figure 3(a)), which should involve the formation of “weak” struts in the final scaffold.

The significantly higher mechanical strength of GC-CEL2 scaffolds in comparison to that of Bioglass<sup>®</sup>-derived ones (Table 4) cannot be attributed only to a slight decrease of pore content, which is almost negligible, but mainly to a better densification of the GC-CEL2 scaffold trabeculae. In fact, as previously discussed in the section “Sintering and crystallization of the glasses: quantitative considerations”, CEL2 exhibits a significantly higher Hruby parameter (Table 3) as well as a greater sinterability in comparison to Bioglass<sup>®</sup>, which eventually leads to scaffolds with well-densified and strengthened struts.

The different compressive strength of the scaffolds can be also dependent on the intrinsic characteristics of the material constituting the porous body – for instance, different mechanical strength and hardness of the crystalline phases detected in sintered GC-CEL2 and GC-Bioglass<sup>®</sup>. Definite, quantitative assessment of the relationship between the mechanical properties of the crystalline phases and those of the scaffolds – i.e., the correlation between macro- and micromechanics of the scaffolds – goes beyond the aim of the present work. However, we wish to present the following, simple reasoning: in principle, higher the density of a material, higher is its mechanical strength; therefore, we can compare the densities of the crystalline phases detected by XRD in GC-CEL2 and GC-Bioglass<sup>®</sup> scaffolds. By looking at the data available in the PDF database, we observed that the densities of  $\text{Na}_2\text{CaSi}_2\text{O}_6$  (major crystalline phase of GC-Bioglass<sup>®</sup>),  $\text{Na}_4\text{Ca}_4(\text{Si}_6\text{O}_{18})$  and  $\text{Ca}_2\text{Mg}(\text{Si}_2\text{O}_7)$  (both found in GC-CEL2) are  $\sim 2.83$ ,  $\sim 2.85$  and  $\sim 2.95 \text{ g}\cdot\text{cm}^{-3}$ , respectively. The densities of GC-CEL2 crystalline phases are higher in comparison to that of GC-Bioglass<sup>®</sup> phase, and the mechanical strength of the two types of scaffolds are affected accordingly. It is worth highlighting that the GC-BG32 and GC-BG5 scaffolds produced in this work are the first Bioglass<sup>®</sup>-derived porous bodies able to exhibit suitable mechanical properties and porous

architecture for really deeming a final clinical use of them. Foam-derived GC-Bioglass<sup>®</sup> scaffolds previously described in the literature, even though exhibiting suitable pore content for potential bone tissue in-growth and excellent bioactivity, were too brittle to be safely implanted *in vivo* [16,17]. Fabrication of GC-Bioglass<sup>®</sup> scaffolds with higher strength (up to 7 MPa) was reported by Wu et al. [18], but they were characterized by a poorly interconnected pore network and a too low pore content (~45 %vol.) to be actually suggested as suitable bone grafts. Table 5 provides an useful comparison between the properties of the scaffolds produced in the present work and those of some glass/glass-ceramic scaffolds, all fabricated by sponge replication, proposed in the literature [16,17,21,23,36-43]. It is worth underlining that all these scaffolds exhibit very attractive architectural features (e.g. adequate pore content, bone-like trabecular structure) and bioactive properties, but only a subset of them [21,36-42] possesses mechanical strength comparable to that of cancellous bone (2-12 MPa [1]).

A comparison among typical stress-strain curves of the scaffolds produced in the present work is reported in Figure 13; especially for GC-BG5-1100 and GC-CEL2 scaffolds, a multi-peak profile of the curves is clearly evident. The curves have a positive slope up to a first peak, after which the scaffold's thinner struts begin to crack causing an apparent stress drop (negative slope); however, the scaffold was still able to bear higher loads and therefore the stress rises again. The repetition of this behaviour gave a jagged stress-strain curve while the progressive cracking of scaffold's trabeculae occurs; finally, when also the thicker struts are fractured, the curve has an ultimate negative slope. This behaviour, typical for foam-like solids, was also observed by other authors, such as Jones et al. [44] and Chen et al. [16], for glass-ceramic scaffolds.

A few considerations about the relationship between scaffold strength and porosity are also presented as closing remarks. The scaffolds prepared in this work were all produced by the same fabrication method (sponge replication) and, therefore, their trabecular architecture can be considered quite similar. Hence, by adopting a remarkable simplification, it is possible to hypothesize that, for the same glass composition and particles size, the scaffold strength is only

dependent on pore content ( $P$ ) *per se*. Therefore, the scaffold compressive strength can be related to  $P$  by means of an empirical function ( $\sigma^*$ ) interpolating the measured values; the coefficient of determination  $R^2$  gives an evaluation about the “goodness of fitting” of the model. Comparison among the fitting curves interpolating the data from GC-B5-1100, GC-BG32-1180 and GC-CEL2 scaffolds is reported in Figure 14; we did not consider those Bioglass<sup>®</sup>-derived scaffold batches characterized by incomplete sintering of the struts (Figures 9(a)-(f)), which involves that scaffold strength is not dependent only by pore content *per se* but is also negatively affected by a high intrinsic brittleness of scaffold struts.

The curve  $\sigma_{GC-BG5}^*$  could be interpreted as the results of a rigid, upward translation of the curve  $\sigma_{GC-BG32}^*$ ; from the viewpoint of scaffold processing, this effect is regulated by the size of starting Bioglass<sup>®</sup> particles. The different slopes of the  $\sigma_{GC-CEL2}^*$  and  $\sigma_{GC-BG32}^*$  curves (the starting glass particles were sieved below 32  $\mu\text{m}$  in both cases) can be attributable to different intrinsic properties of the materials (the “material effect”), such as the different micromechanical features of the crystalline phases of GC-CEL2 and GC-BG32. Increment of the strength of GC-CEL2 scaffolds is higher than that of GC-Bioglass<sup>®</sup> scaffolds when porosity decreases, i.e. when the “material effect” plays a more significant role.

As a general comment, a negative linear relationship between scaffold porosity and compressive strength can be found, with  $R^2$  above 0.80 (Figure 14(a)). Gerhardt and Boccaccini [45] showed that linear interpolation usually offers an acceptable approximation to describe the relationship between scaffold compressive strength and porosity, except for highly-porous Bioglass<sup>®</sup>-derived scaffolds [16] due to the onset of instability phenomena related to their high brittleness. Hellmich and co-workers [46,47] developed micromechanical models of porous ceramics and found that non-linear strength-porosity relations are in very good accordance with experimental results. Baino et al. [48] suggested that a good fitting of experimental data can be obtained by using second order polynomial functions; interpolation of experimental data by a quadratic model is reported in Figure

14(b). It is worth underlining that, as expected,  $R^{2,quadr} > R^{2,lin}$  for all the considered scaffold batches.

### *In vitro bioactivity*

*In vitro* bioactivity of sintered Bioglass<sup>®</sup> in form of both bulk samples and porous scaffolds was investigated in detail elsewhere [8,16,49].

As a representative example, the results of *in vitro* tests carried out on a GC-BG32-1180 scaffold after immersion for 7 days in SBF are shown in Figure 15. Scaffold struts are homogeneously and continuously coated by a newly formed phase constituted by globe-shaped agglomerates (Figure 15(a)), whose “cauliflower morphology” is typical of apatite phase(s) grown on the surface of bioactive glasses. Compositional analysis (Figure 15(b)) confirmed the calcium-phosphate nature of this layer, that revealed a molar ratio Ca/P = 1.65. Ca/P ratio is slightly lower than the theoretical one of natural HA (1.67) because the newly formed apatite phase is a mixture of amorphous and crystalline calcium phosphate, as suggested in other reports [16]. The peak of silicon (Si) visible in Figure 15(b) is attributable to the residual silica gel lying underneath the HA layer, according to the bioactivity mechanism proposed by Hench [1,4], whereas the presence of silver (Ag) peaks is due to the metal coating necessary for EDS analysis.

After soaking in SBF, GC-BG32-1180 were also embedded in epoxy resin (Struers Epofix), cut and carefully polished by using SiC grit (from #600 to #4000) papers; one of the resulting cross-sections is shown in Figure 15(c): the back-scattered mode adopted for this SEM analysis emphasizes the presence of the apatite layer grown on scaffold walls, as indicated in the picture (dark grey layer); the newly formed layer is compact, continuous and constitutes a thick “skin” (up to ~50 µm) on scaffold struts.

The high bioactive behaviour of GC-BG32 scaffolds sintered at 1180 °C for 3 h is an important finding that expands the observations performed by other authors. In 1992, Li et al. [50] reported that crystallization of Bioglass<sup>®</sup> turns the bioactive glass into a inert-like material. More recently,

this crucial issue was investigated in detail by Peitl et al. [51] and Clupper et al. [49], who reported quantitative investigations about the relationship between crystallinity of Bioglass<sup>®</sup>-derived glass-ceramics and kinetics of apatite formation *in vitro*. The major crystalline phase Na<sub>2</sub>Ca<sub>2</sub>Si<sub>3</sub>O<sub>9</sub>, that nucleates during the process of sintering, decreases the kinetics of formation of HA on the Bioglass<sup>®</sup>-derived glass-ceramics, but does not totally suppress the growth of this bioactive layer. In this context, a further point should be underlined: surface reaction kinetics of a highly porous body (in this case a glass-ceramic scaffold) are faster than those of a dense product with analogous chemical/structural composition due to its higher surface area available for ion-exchange phenomena.

Comparing the SEM images reported in Figures 15(c),(d), the *in vitro* bioactivity of GC-CEL2 scaffold seems to be higher than that of GC-BG32-1180 sample, as evident from the difference of thickness of HA layer formed on the struts of the two scaffolds. In the present work, the maximum thickness of the HA layer (~50 and ~75 μm for GC-BG32-1180 and GC-CEL2 scaffolds, respectively), measured by using a proper tool of the SEM software, was assumed as a preliminary index to quantify and compare the *in vitro* bioactivity of the scaffolds. The kinetics of *in vitro* apatite formation on GC-CEL2 scaffold struts were recently investigated in more detail by Renghini et al. [52].

The presence of an apatite/HA layer on scaffold struts plays a key role for promoting the graft colonization by bone cells. It was demonstrated that osteoblasts attach preferably on HA agglomerates due to HA chemical and crystallographic similarity to bone mineral [23]. Under this viewpoint, apatite layer can be viewed as a “biomimetic skin” making the scaffold struts surface a highly biocompatible substrate apt for cells adhesion *in vitro* and *in vivo*.



## CONCLUSIONS

In this work, Bioglass<sup>®</sup> - and CEL2-derived glass-ceramic scaffolds were fabricated through sponge replication technique by an optimized schedule. Foam-like highly porous (~70 %vol.) scaffolds with mechanical strength (~2.5 MPa) actually comparable to that of cancellous bone were produced for the first time from commercial Bioglass<sup>®</sup> powders. In fact, by carefully designing the processing parameter and the sintering conditions, excellent densification of scaffold struts were achieved, which imparted high-strength properties to the final sintered scaffold. This is a significant finding in the context of biomaterials for bone tissue engineering and opens new perspectives towards a truly functional bone substitute suitable for clinical use. Comparing the features of Bioglass<sup>®</sup> - and CEL2-derived scaffolds, the latter exhibited a mechanical strength ( $4.5 \pm 0.9$  MPa) twice that of the former, although both had the same pore content (~70 %vol.); this was due to the different sintering behaviour of the two glasses and to the features of the different crystalline phases in the glass-ceramic scaffolds (“material effect”). All scaffolds exhibited a trabecular architecture mimicking that of spongy bone, with a highly interconnected network of open macropores in the 100-600  $\mu\text{m}$  range. Formation of a thick (up to ~50 and ~75  $\mu\text{m}$  for Bioglass<sup>®</sup> - and CEL2-derived scaffolds, respectively) and continuous apatite layer on pore walls after *in vitro* tests (soaking for 7 days in SBF) demonstrated the excellent bioactivity of all produced scaffolds. Considering their bioactive, architectural and mechanical features, the optimized Bioglass<sup>®</sup> - and CEL2-based scaffolds can be suggested as effective implants for bone substitution.

## ACKNOWLEDGMENTS

Regione Piemonte (Ricerca Sanitaria Finalizzata 2006 and 2008) are kindly acknowledged for supporting this research work.

## REFERENCES

1. Hench, L.L. Bioceramics: From Concept to Clinic, *J. Am. Ceram. Soc.*, 1991: **74**: 1487-1510.
2. Cao, W. and Hench, L.L. Bioactive Materials, *Ceram. Int.*, 1996: **22**: 493-507.
3. Hench, L.L. Biomaterials: A Forecast for the Future, *Biomaterials*, 1998: **19**: 1419-1423.
4. Hench, L.L. Bioceramics, *J. Am. Ceram. Soc.*, 1998: **81**: 1705-1727.
5. Dorozhkin, S.V. Bioceramics of Calcium Orthophosphates, *Biomaterials*, 2010: **31**: 1465-1485.
6. Daculsi, G., Laboux, O., Malard, O. and Weiss, P. Current State of the Art of Biphasic Calcium Phosphate Bioceramics, *J. Mater. Sci.: Mater. Med.*, 2003: **14**: 195-200.
7. Benaqqa, C., Chevalier, J., Saadaoui, M. and Fantozzi, G. Slow Crack Growth Behaviour of Hydroxyapatite Ceramics, *Biomaterials*, 2005: **26**: 6106-6112.
8. Hench, L.L. The Story of Bioglass<sup>®</sup>, *J. Mater. Sci.: Mater. Med.*, 2006: **17**: 967-978.
9. Jones, J.R., Gentleman, E. and Polak, J. Bioactive Glass Scaffolds for Bone Regeneration, *Elements*, 2007: **3**: 393-399.
10. Chevalier, J. and Gremillard, L. Ceramics for Medical Applications: A Picture for the Next 20 Years, *J. Eur. Ceram. Soc.*, 2009: **29**: 1245-1255.
11. Hench, L.L., Splinter, R.J., Allen, W.C. and Greenlee, T.K. Bonding Mechanisms at the Interface of Ceramic Prosthetic Materials, *J. Biomed. Mater. Res.*, 1972: **2**: 117-141.
12. Baino, F. and Vitale-Brovarone, C. Three-dimensional Glass-Derived Scaffolds for Bone Tissue Engineering: Current Trends and Forecasts for the Future, *J. Biomed. Mater. Res. A*, 2011: **97**: 514-535.
13. Xynos, I.D., Edgar, A.J., Buttery, L.D., Hench, L.L. and Polak, J.M. Gene-Expression Profiling of Human Osteoblasts Following Treatment with the Ionic Products of Bioglass 45S5 Dissolution, *J. Biomed. Mater. Res.*, 2001: **55**: 151-157.
14. Hench, L.L. Genetic Design of Bioactive Glasses, *J. Eur. Ceram. Soc.*, 2009: **29**: 1257-1265.

15. Hoppe, A., Guldal, N.S. and Boccaccini, A.R. A Review of the Biological Response to Ionic Dissolution Products from Bioactive Glasses and Glass-Ceramics, *Biomaterials*, 2011: **32**: 2757-2774.
16. Chen, Q.Z., Thompson, I.D. and Boccaccini, A.R. 45S5 Bioglass<sup>®</sup>-Derived Glass-Ceramic Scaffolds for Bone Tissue Engineering, *Biomaterials*, 2006: **27**: 2414-2425.
17. Bretcanu, O., Chen, Q., Misra, S.K., Boccaccini, A.R., Verné, E. and Vitale-Brovarone, C. Biodegradable Polymer Coated 45S5 Bioglass-Derived Glass-Ceramic Scaffolds for Bone Tissue Engineering, *Glass Tech. Eur. J.: Glass Sci. Tech. A*, 2007: **48**: 227-234.
18. Wu, S.C., Hsu, H.C., Hsiao, S.H. and Ho, W.F. Preparation of Porous 45S5 Bioglass<sup>®</sup>-Derived Glass-Ceramic Scaffolds by Using Rice Husk as a Porogen Additive, *J. Mater. Sci.: Mater. Med.*, 2009: **20**: 1229-1236.
19. Karageorgiou, V. and Kaplan, D. Porosity of 3D Biomaterial Scaffolds and Osteogenesis, *Biomaterials*, 2005: **26**: 5474-5491.
20. Bellucci, D., Cannillo, V. and Sola, A. Shell Scaffolds: A New Approach towards High Strength Bioceramic Scaffolds for Bone Regeneration, *Mater. Lett.*, 2010: **64**: 203-206.
21. Vitale-Brovarone, C., Baino, F. and Verné, E. High Strength Bioactive Glass-Ceramic Scaffolds for Bone Regeneration, *J. Mater. Sci.: Mater. Med.*, 2009: **20**: 643-653.
22. Vitale-Brovarone, C., Verné, E., Robiglio, L., Martinasso, G., Canuto, R.A. and Muzio, G. Biocompatible Glass-Ceramic Materials for Bone Substitution, *J. Mater. Sci.: Mater. Med.*, 2008: **19**: 471-478.
23. Vitale-Brovarone, C., Verné, E., Robiglio, L., Appendino, P., Bassi, F., Martinasso, G., Muzio, G. and Canuto, R. Development of Glass-Ceramic Scaffolds for Bone Tissue Engineering: Characterisation, Proliferation of Human Osteoblasts and Nodule Formation, *Acta Biomater.*, 2007: **3**: 199-208.
24. Kokubo, T. and Takadama, H. How Useful Is SBF in Predicting In Vivo Bone Bioactivity?, *Biomaterials*, 2006: **27**: 2907-2915.

25. Erol, M., Kucukbayrak, S. and Ersoy-Mericboyu, A. Influence of Particle Size on the Crystallization Kinetics of Glasses Produced from Waste Materials, *J. Non-Cryst. Solids*, 2011: **357**: 211-219.
26. Bretcanu, O., Chatzistavrou, X., Paraskevopoulos, K., Conradt, R., Thompson, I. and Boccaccini, A.R. Sintering and Crystallization of 45S5 Bioglass<sup>®</sup> Powder, *J. Eur. Ceram. Soc.*, 2009: **29**: 3299-3306.
27. Huang, R., Pan, J., Boccaccini, A.R. and Chen, Q.Z. A Two-Scale Model for Simultaneous Sintering and Crystallization of Glass–Ceramic Scaffolds for Tissue Engineering, *Acta Biomater.*, 2008: **4**: 1095-1103.
28. Hruby, A. Evaluation of Glass-Forming Tendency by Means of DTA, *Czech. J. Phys.*, 1972: **22**: 1187-1193.
29. Panda, P.C. and Raj, R. Sintering and Crystallization of Glass at Constant Heating Rate, *J. Am. Ceram. Soc.*, 1989: **69**: 1564-1566.
30. Ferraris, M. and Verné, E. Viscous Phase Sintering of Particle-Reinforced Glass Matrix Composites, *J. Eur. Ceram. Soc.*, 1996: **16**: 421-427.
31. Lara, C., Pascual, M.J. and Duran, A. Glass-Forming Ability, Sinterability and Thermal Properties in The System RO-BaO-SiO<sub>2</sub> (R = Mg, Zn), *J. Non-Cryst. Solids*, 2004: **348**: 149-155.
32. Lin, C.C., Huang, L.C. and Shen, P. Na<sub>2</sub>CaSi<sub>2</sub>O<sub>6</sub>-P<sub>2</sub>O<sub>5</sub> Based Bioactive Glasses. Part I: Elasticity and Structure, *J. Non-Cryst. Solids*, 2005: **351**: 3195-3203.
33. Lefebvre, L., Chevalier, J., Gremillard, L., Zenati, R., Thollet, G., Bernache-Assolant, D. and Govin, A. Structural Transformation of Bioactive Glass 45S5 with Thermal Treatments, *Acta Mater.*, 2007: **55**: 3305-3313.
34. Lefebvre, L., Gremillard, L., Chevalier, J., Zenati, R. and Bernache-Assolant, D. Sintering Behaviour of 45S5 Bioactive Glass, *Acta Biomater.*, 2008: **4**: 1894-1903.

35. Bellucci, D., Cannillo, V., Sola, A., Chiellini, F., Gazzarri, M. and Migone, C. Macroporous Bioglass<sup>®</sup>-Derived Scaffolds for Bone Tissue Regeneration, *Ceram. Int.*, 2011: **37**: 1575-1585.
36. Vitale-Brovarone, C., Bairo, F., Bretcanu, O. and Verné, E. Foam-Like Scaffolds for Bone Tissue Engineering Based on a Novel Couple of Silicate-Phosphate Specular Glasses: Synthesis and Properties, *J. Mater. Sci.: Mater. Med.*, 2009: **20**: 2197-2205.
37. Vitale-Brovarone, C., Bairo, F. and Verné, E. Feasibility and Tailoring of Bioactive Glass-ceramic Scaffolds with Gradient of Porosity for Bone Grafting, *J. Biomater. Appl.*, 2010: **24**: 693-712.
38. Vitale-Brovarone, C., Miola, M., Balagna, C. and Verné, E. 3D Glass-Ceramic Scaffolds with Antibacterial Properties for Bone Grafting, *Chem. Eng. J.*, 2008: **137**: 129-136.
39. Balagna, C., Vitale-Brovarone, C., Miola, M., Canuto, R.A., Saracino, S., Muzio, G., Fucile, G., Maina, G. and Verné, E. Biocompatibility and Antibacterial Effect of Silver Doped 3D-Glass-Ceramic Scaffolds for Bone Grafting, *J. Biomater. Appl.*, 2011: **25**: 595-617.
40. Fu, Q., Rahaman, M.N., Sonny Bal, B., Brown, R.F. and Day, D.E. Mechanical and In Vitro Performance of 13-93 Bioactive Glass Scaffolds Prepared by a Polymer Foam Replication technique, *Acta Biomater.*, 2008: **4**: 1854-1864.
41. Fu, H., Fu, Q., Zhou, N., Huang, W., Rahaman, M.N., Wang, D. and Liu, X. In Vitro Evaluation of Borate-Based Bioactive Glass Scaffolds Prepared by a Polymer Foam Replication Method, *Mater. Sci. Eng. C*, 2009: **29**: 2275-2281.
42. Liu, X., Huang, W., Fu, H., Yao, A., Wang, D., Pan, H. and Lu, W.W. Bioactive Borosilicate Glass Scaffolds: Improvement on the Strength of Glass-Based Scaffolds for Tissue Engineering, *J. Mater. Sci.: Mater. Med.*, 2009: **20**: 365-372.
43. Vitale-Brovarone, C., Ciapetti, G., Leonardi, E., Baldini, N., Bretcanu, O., Verné, E. and Bairo, F. Resorbable Glass-Ceramic Phosphate-Based Scaffolds for Bone Tissue

- Engineering: Synthesis, Properties and In Vitro Effects on Human Marrow Stromal Cells, *J. Biomater. Appl.*, in press. DOI: 10.1177/0885328210372149.
44. Jones, J.R., Ehrenfried, L.M. and Hench, L.L. Optimising Bioactive Glass Scaffolds for Bone Tissue Engineering, *Biomaterials*, 2006: **27**: 964-973.
  45. Gerhardt, L.C. and Boccaccini, A.R. Bioactive Glass and Glass-Ceramic Scaffolds for Bone Tissue Engineering, *Materials*, 2010: **3**: 3867-3910.
  46. Fritsch, A., Dormieux, L., Hellmich, C. and Sanahuja, J. Mechanical Behavior of Hydroxyapatite Biomaterials: An Experimentally Validated Micromechanical Model for Elasticity and Strength, *J. Biomed. Mater. Res. A*, 2007: **88**: 149-161.
  47. Malasoma, A., Fritsch, A., Kohlhauser, C., Brynk, T., Vitale-Brovarone, C., Pakiela, Z., Eberhardsteiner, J. and Hellmich, C. Micromechanics of Bioresorbable Porous CEL2 Glass Ceramic Scaffolds for Bone Tissue Engineering, *Adv. Appl. Ceram.*, 2008: **107**: 277-286.
  48. Baino, F., Verné, E. and Vitale-Brovarone, C. 3-D High Strength Glass-Ceramic Scaffolds Containing Fluoroapatite for Load-Bearing Bone Portions Replacement, *Mater. Sci. Eng. C*, 2009: **29**: 2055-2062.
  49. Clupper, D.C., Mecholsky, J.J. Jr., LaTorre, G.P. and Greenspan, D.C. Bioactivity of Tape Cast and Sintered Glass-Ceramic in Simulated Body Fluid, *Biomaterials*, 2002: **23**: 2599-2606.
  50. Li, P., Zhang, F. and Kokubo, T. The Effect of Residual Glassy Phase in a Bioactive Glass-Ceramic on the Formation of its Surface Apatite Layer In Vitro, *J. Mater. Sci.: Mater. Med.*, 1992: **3**: 452-456.
  51. Peitl, F.O., LaTorre, G.P. and Hench, L.L. Effect of Crystallization on Apatite-Layer Formation of Bioactive Glass 45S5, *J. Biomed. Mater. Res.*, 1996: **30**: 509-514.
  52. Renghini, C., Komlev, V., Fiori, F., Verné, E., Baino, F. and Vitale-Brovarone, C. Micro-CT Studies on 3-D Bioactive Glass-Ceramic Scaffolds for Bone Regeneration, *Acta Biomater.*, 2009: **5**: 1328-1337.

## Tables

*Table 1. Composition of starting glasses.*

Glass	Composition (%mol.)					
	SiO <sub>2</sub>	P <sub>2</sub> O <sub>5</sub>	CaO	Na <sub>2</sub> O	MgO	K <sub>2</sub> O
Bioglass <sup>®</sup>	46.1	2.6	26.9	24.4	-	-
CEL2	45.0	3.0	26.0	15.0	7.0	4.0

*Table 2. Preparation of starting glasses.*

Glass	Raw products	Melting conditions
Bioglass <sup>®</sup>	SiO <sub>2</sub> , Ca <sub>3</sub> (PO <sub>4</sub> ) <sub>2</sub> , CaCO <sub>3</sub> , Na <sub>2</sub> CO <sub>3</sub>	1500 °C for 1 h (heating rate: 10 °C·min <sup>-1</sup> )
CEL2	SiO <sub>2</sub> , Ca <sub>3</sub> (PO <sub>4</sub> ) <sub>2</sub> , CaCO <sub>3</sub> , Na <sub>2</sub> CO <sub>3</sub> , (MgCO <sub>3</sub> ) <sub>4</sub> ·Mg(OH) <sub>2</sub> ·5H <sub>2</sub> O, K <sub>2</sub> CO <sub>3</sub>	1400 °C for 1 h (heating rate: 10 °C·min <sup>-1</sup> )

*Table 3. DTA results (heating rate: 20 °C·min<sup>-1</sup>) and derived thermal parameters.*

Glass	T <sub>g</sub> (°C)	T <sub>x</sub> (°C)	T <sub>c</sub> (°C)	T <sub>x</sub> – T <sub>g</sub> (°C)	K <sub>H</sub>
BG32	553	590	691	37	0.066
BG5	546	588	667	42	0.082
CEL2	552	652; 845	706; 873	100 <sup>a</sup>	0.28 <sup>a</sup>

<sup>a</sup> T<sub>x1</sub> was considered for calculation.

*Table 4. Features of the produced scaffolds (5 samples were tested for each scaffold batch).*

Scaffold	$S_{\text{scaffold}}$ (%)	P (%vol.)	$\sigma_c$ (MPa)
GC-BG32-1100	$20.9 \pm 4.2$	$83.0 \pm 1.0$	$0.2 \pm 0.1$
GC-BG32-1180	$61.6 \pm 5.3$	$70.7 \pm 3.3$	$1.3 \pm 0.8$
GC-BG5-1100	$60.9 \pm 2.4$	$69.3 \pm 2.3$	$2.5 \pm 0.5$
GC-CEL2	$61.9 \pm 4.8$	$66.4 \pm 2.0$	$4.5 \pm 0.9$



*Table 5. Overview of porosity and mechanical properties of select bone tissue engineering glass-derived scaffolds fabricated through sponge replication.*

Scaffold material <sup>a,b</sup>	Remarks	Porosity (% vol.)	Compressive strength (MPa)	References
GC-Bioglass <sup>®</sup>	Starting glass powders size < 5 µm (commercial product). Sintering condition: 1000 °C/1 h	89-92	0.27-0.42	[16]
	Starting glass powders size < 5 µm (commercial product). Sintering condition: 1100 °C/1 h	79-85	~0.2	[17]
	Starting glass powders size < 32 µm (non-commercial product). Sintering conditions: 1100 °C/ 3 h; 1180 °C/3 h	70.7-83.0	0.2-1.3	Present work
	Starting glass powders size < 5 µm (commercial product). Sintering condition: 1100 °C/3 h	69.3	2.5	Present work
Poly(3-hydroxybutyrate)-coated GC-Bioglass <sup>®</sup>	Composite scaffold	79-85	0.3-1.5	[17]
GC-CEL2	Starting glass powders size < 32 µm. Sintering conditions: 950 °C/3 h; 1000 °C/3 h	55-75	1.0-5.5	[21,23,36]
		~66.4	~4.5	Present work
	Starting glass powders size < 32 µm. Sintering conditions:	~64.6	~1.9	[37]

	1000 °C/3 h. Totally porous scaffold with gradient of porosity			
	Starting glass powders size < 32 µm. Sintering conditions: 1000 °C/3 h. Graded scaffold mimicking the cancellous/cortical bone system (sponge replication was used to fabricate the porous region)	~53.0	~9.7	[37]
GC-FaGC	FaGC composition (%mol.): 50SiO <sub>2</sub> -18CaO-7Na <sub>2</sub> O-6P <sub>2</sub> O <sub>5</sub> -7K <sub>2</sub> O-3MgO-9CaF <sub>2</sub> Starting glass powders size < 32 µm Sintering condition: 700 °C/ 1 h	~75	~2	[38,39]
13-93	13-93 composition (%mol.): 6Na <sub>2</sub> O-12K <sub>2</sub> O-5MgO-20CaO-53SiO <sub>2</sub> -4P <sub>2</sub> O <sub>5</sub> Starting glass powders size: 5-10 µm Sintering condition: 700 °C/ 1 h	~85	~11	[40]
13-93B2	13-93B2 composition (%mol.): 6Na <sub>2</sub> O-8K <sub>2</sub> O-8MgO-22CaO-36B <sub>2</sub> O <sub>3</sub> -18SiO <sub>2</sub> -2P <sub>2</sub> O <sub>5</sub> Starting glass powders size < 53 µm Sintering condition: 600 °C/ 1 h	67.7-86.7	0.8-9.7	[41,42]

GC-ICEL2	ICEL2 composition (%mol.): 45P <sub>2</sub> O <sub>5</sub> -26CaO-15Na <sub>2</sub> O-3SiO <sub>2</sub> - 4K <sub>2</sub> O-7MgO Starting glass powders size < 32 μm Sintering condition: 610 °C/3 h	~85	~0.4	[36,43]
----------	---------------------------------------------------------------------------------------------------------------------------------------------------------------------------------------------------------------	-----	------	---------

<sup>a</sup> Glass names refer to acronym or denotation introduced in the corresponding reference(s).

<sup>b</sup> If present, the notation “GC-” followed by the name of the glass means that the material is a glass-ceramic derived from the parent glass by means of a thermal treatment above the crystallization temperature.

## Figure

**Figure 1.** Glass powders morphology: (a) BG5 (magnification 2000 $\times$ ), (b) BG32 (magnification 1600 $\times$ ), (c) CEL2 (magnification 1500 $\times$ ).

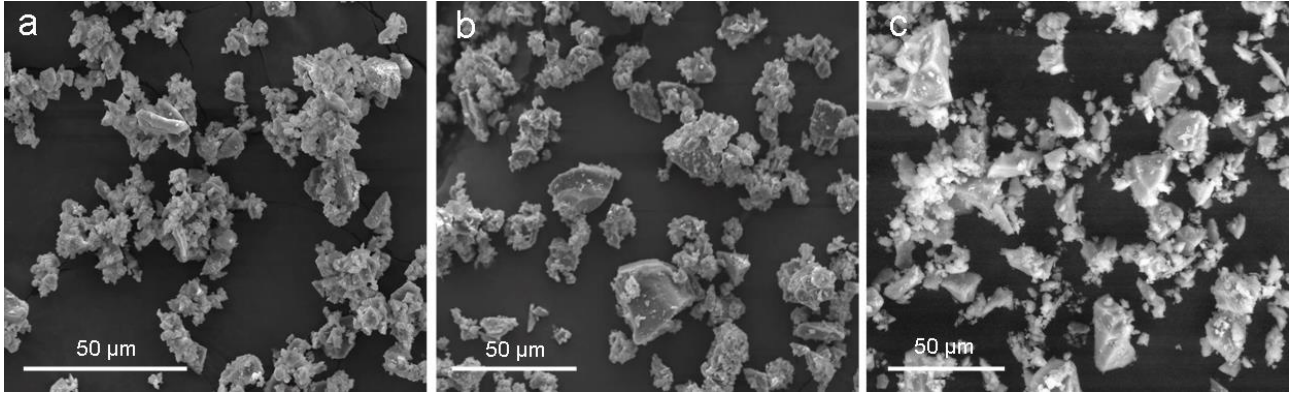


**Figure 2.** HSM images of a cylindrical BG32 sample at different characteristic temperatures during sintering.

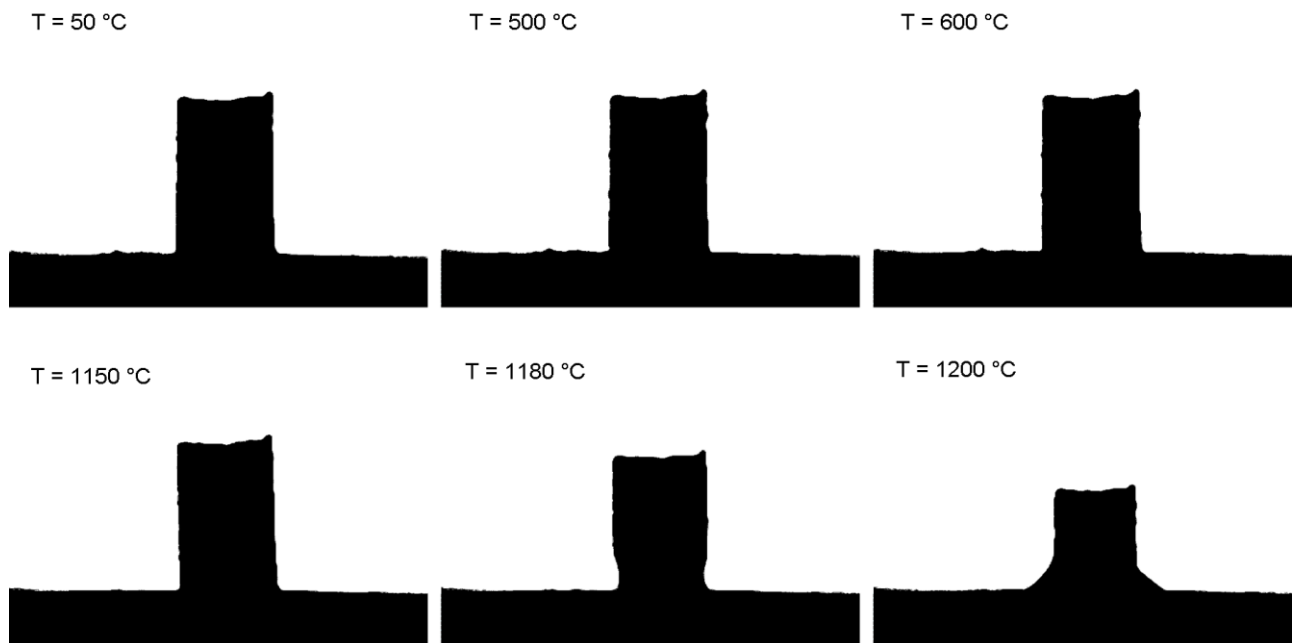


**Figure 3.** Thermal analyses on BG32: (a) shrinkage variation as a function of temperature during HSM and (b) DTA plot.

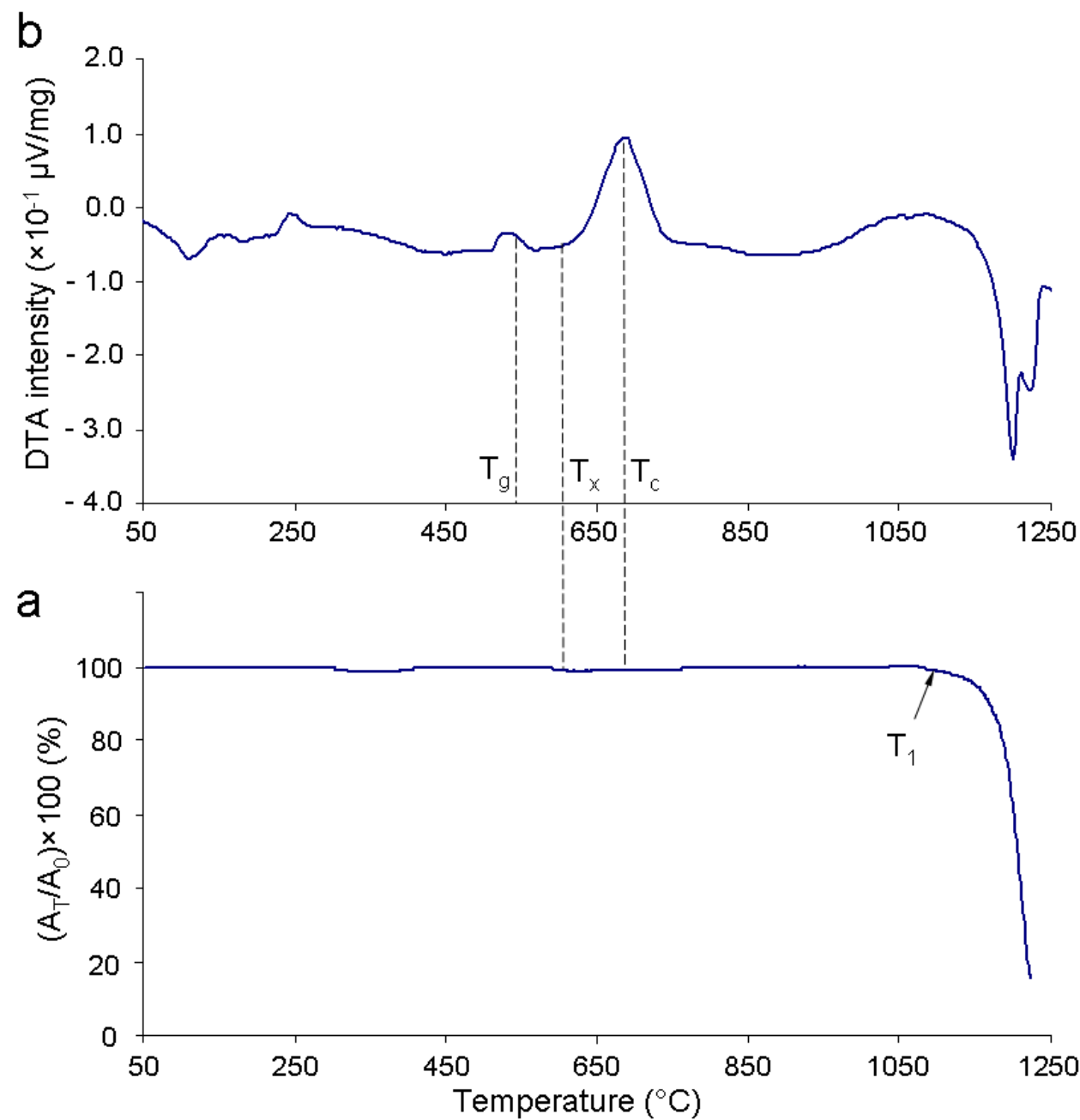


**Figure 4.** HSM images of a cylindrical BG5 sample at different characteristic temperatures during sintering.

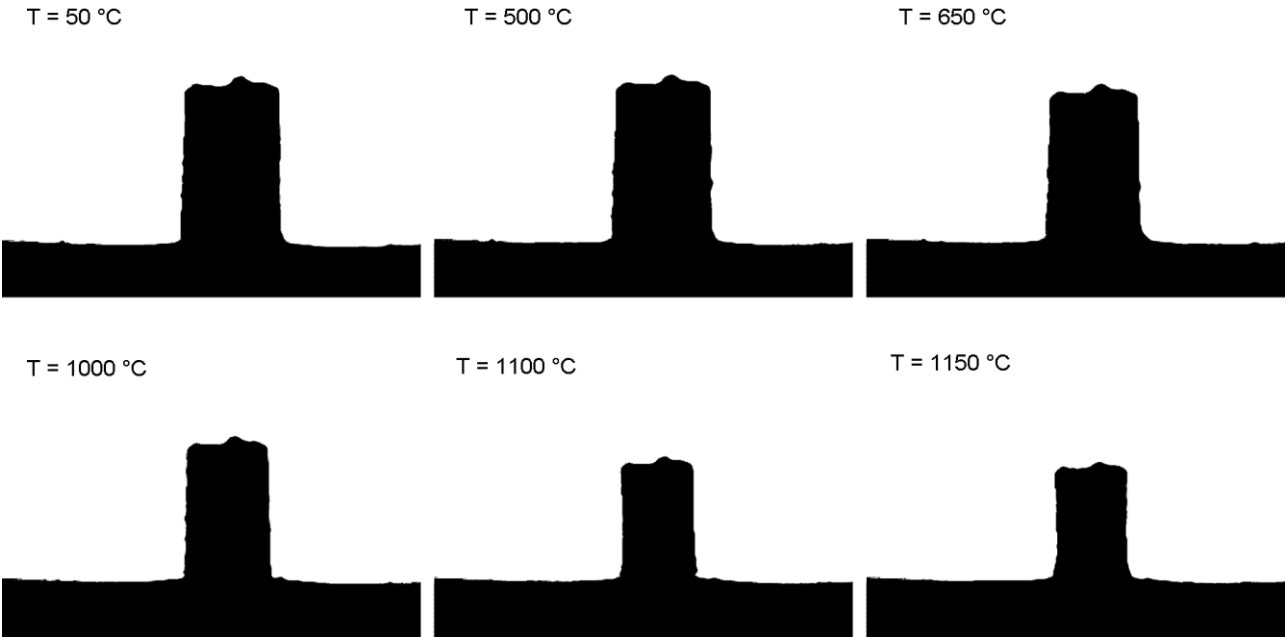


**Figure 5.** Thermal analyses on BG5: (a) shrinkage variation as a function of temperature during HSM and (b) DTA plot.

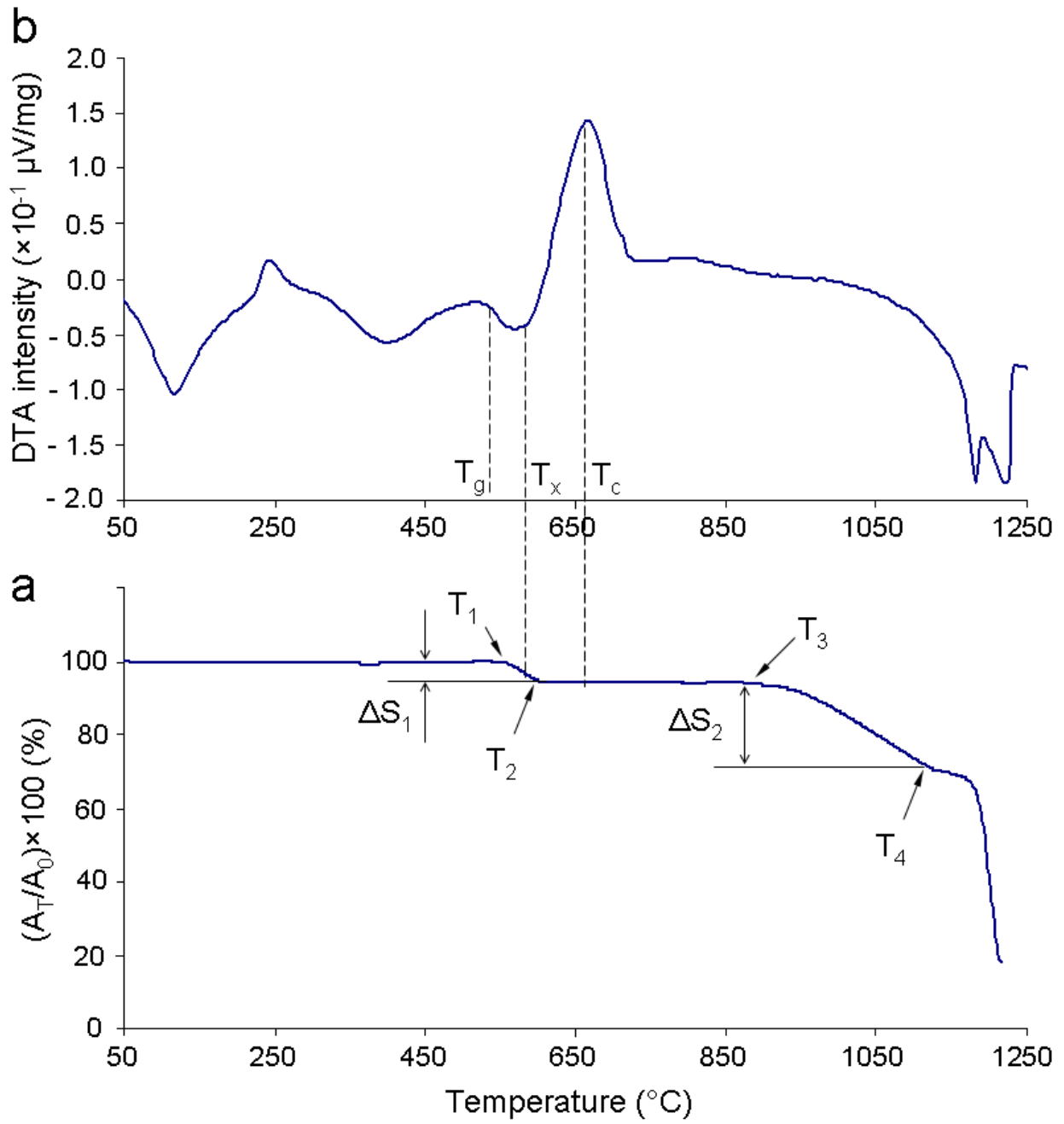


**Figure 6.** HSM images of a cylindrical CEL2 sample at different characteristic temperatures during sintering.

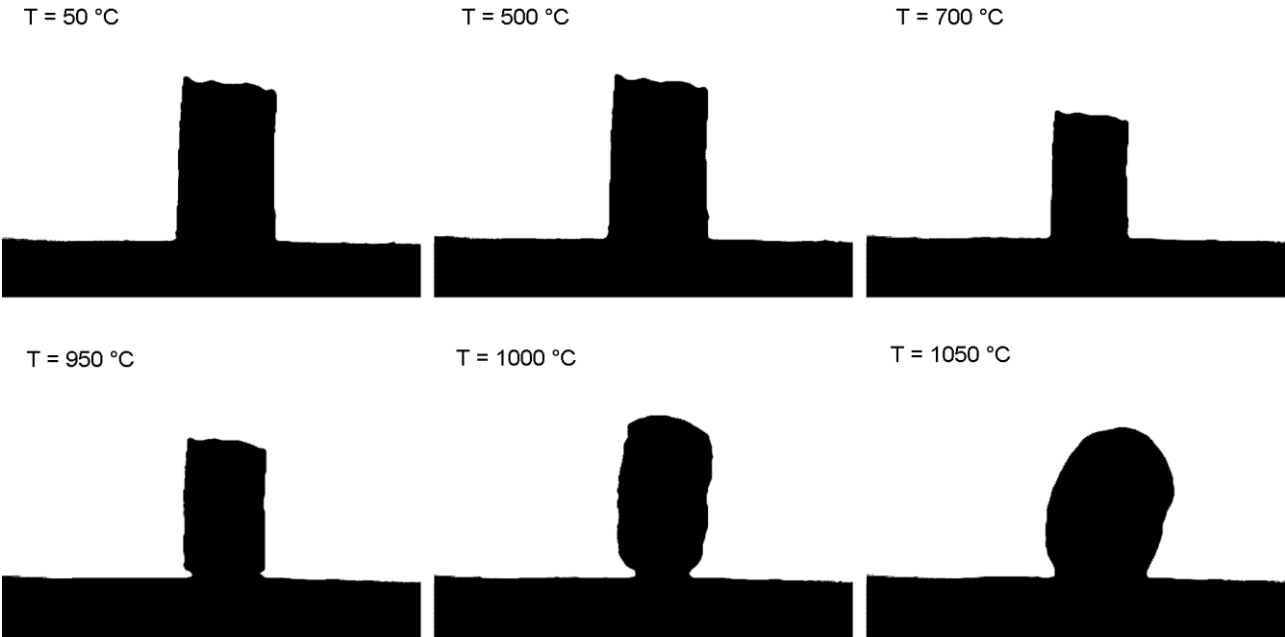




**Figure 7.** Thermal analyses on CEL2: (a) shrinkage variation as a function of temperature during HSM and (b) DTA plot.

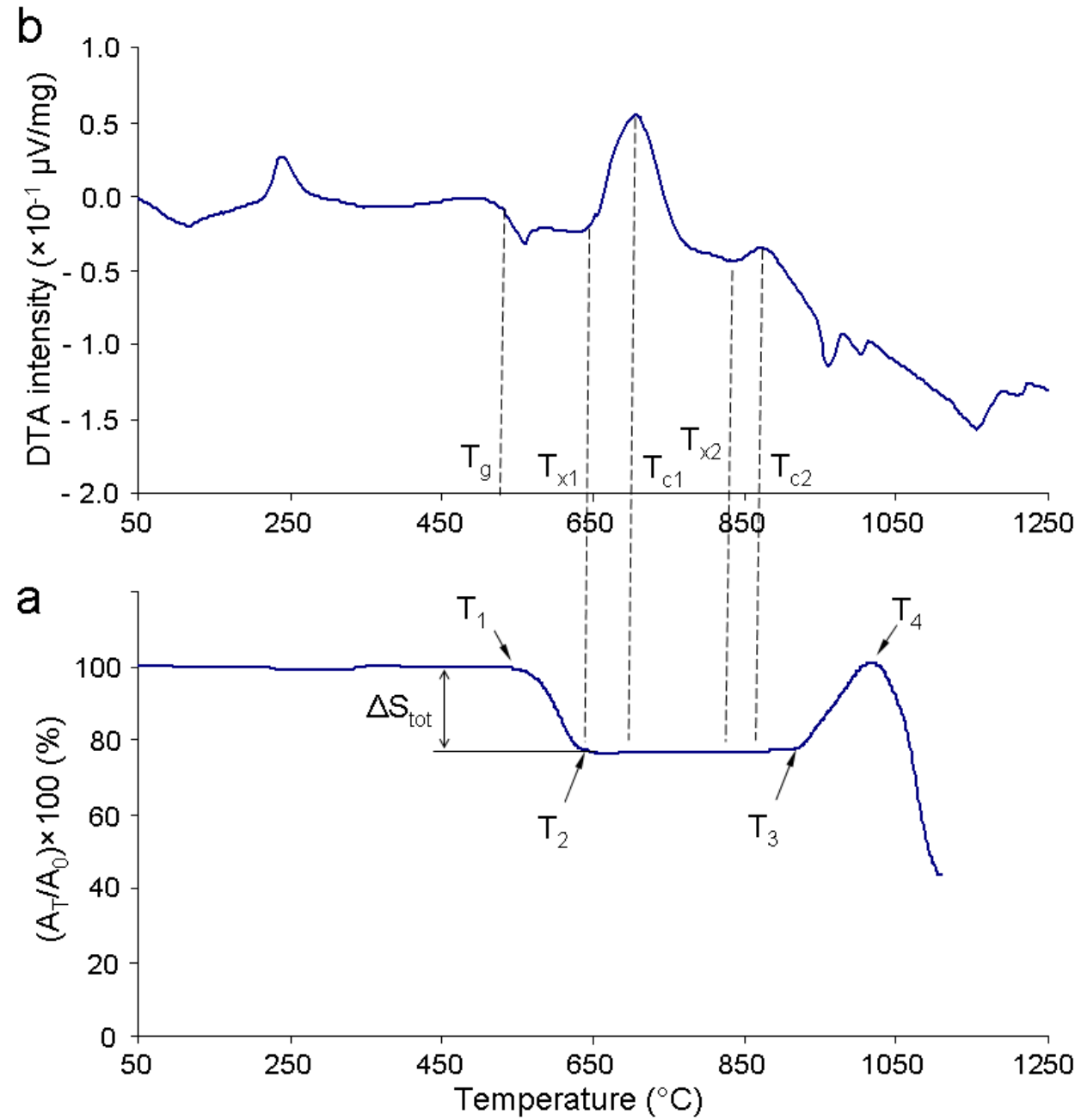


**Figure 8.** WA-XRD patterns of Bioglass<sup>®</sup> powder and Bioglass<sup>®</sup>-derived scaffolds (GC-BG32) ground in powders.

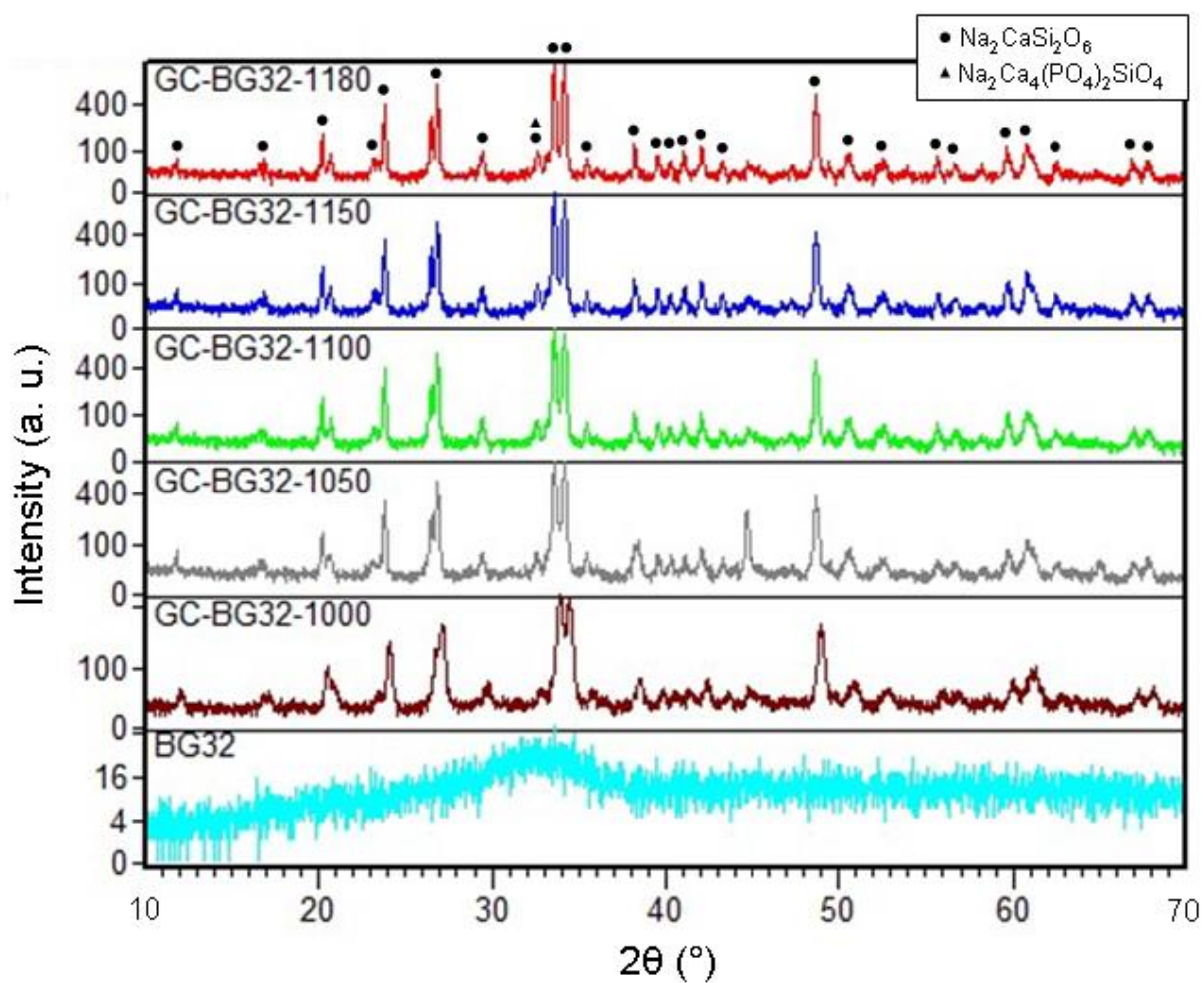


**Figure 9.** GC-BG32 scaffolds architecture: (a) GC-BG32-1000 scaffold (magnification 200 $\times$ ); (b) GC-BG32-1050 scaffold (magnification 300 $\times$ ); (c) GC-BG32-1100 scaffold (magnification 300 $\times$ ); (d) GC-BG32-1150 scaffold (magnification 300 $\times$ ); (e) GC-BG32-1160 scaffold (magnification 400 $\times$ ); (f) GC-BG32-1170 scaffold (magnification 300 $\times$ ); (g-i) GC-BG32-1180 scaffold (magnification 400 $\times$  and 800 $\times$  for (g) and (h), respectively).

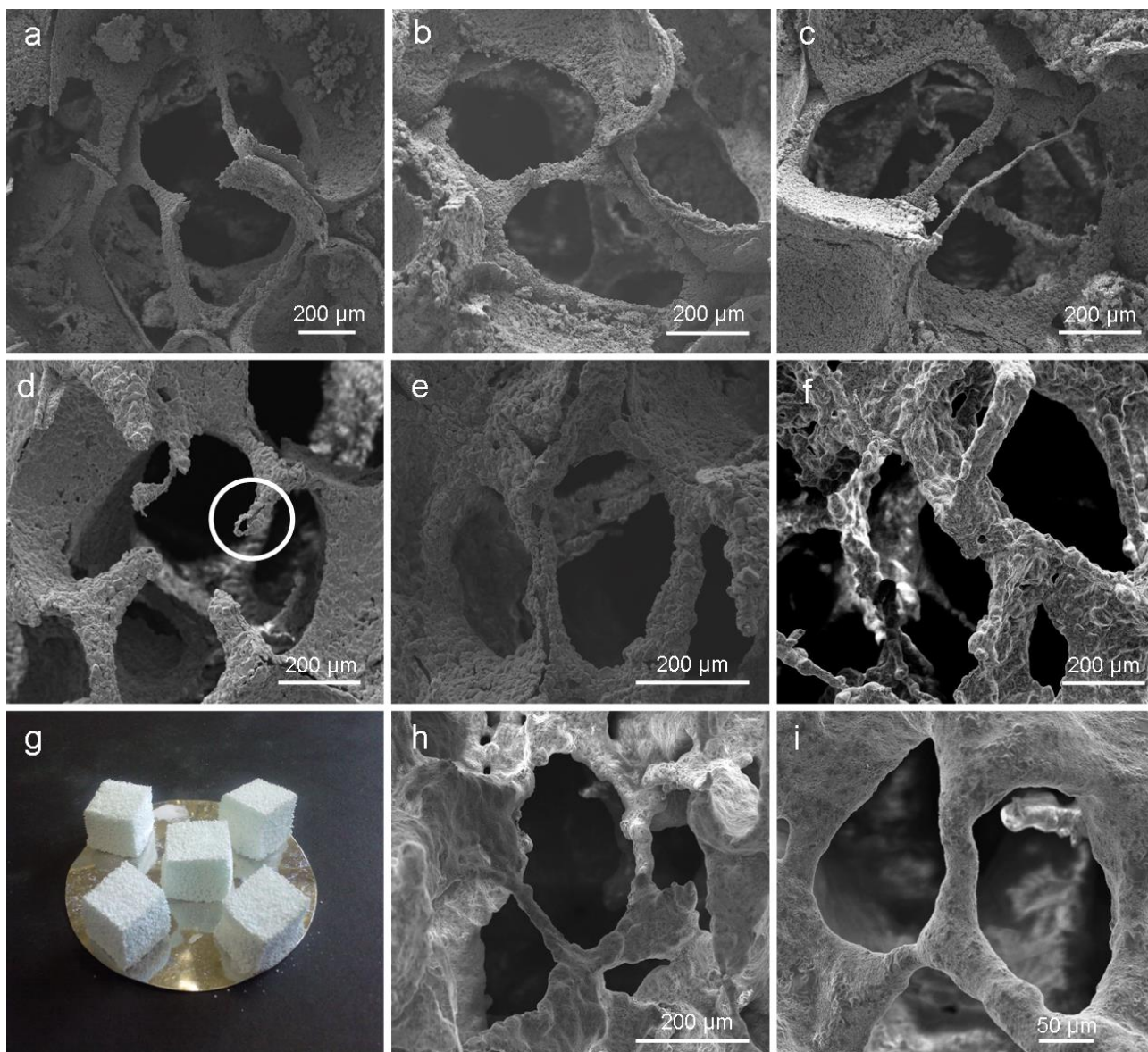


**Figure 10.** SEM micrographs of GC-BG5-1100 scaffold architecture at (a) low magnification (300 $\times$ ) and high magnification (1200 $\times$ ).

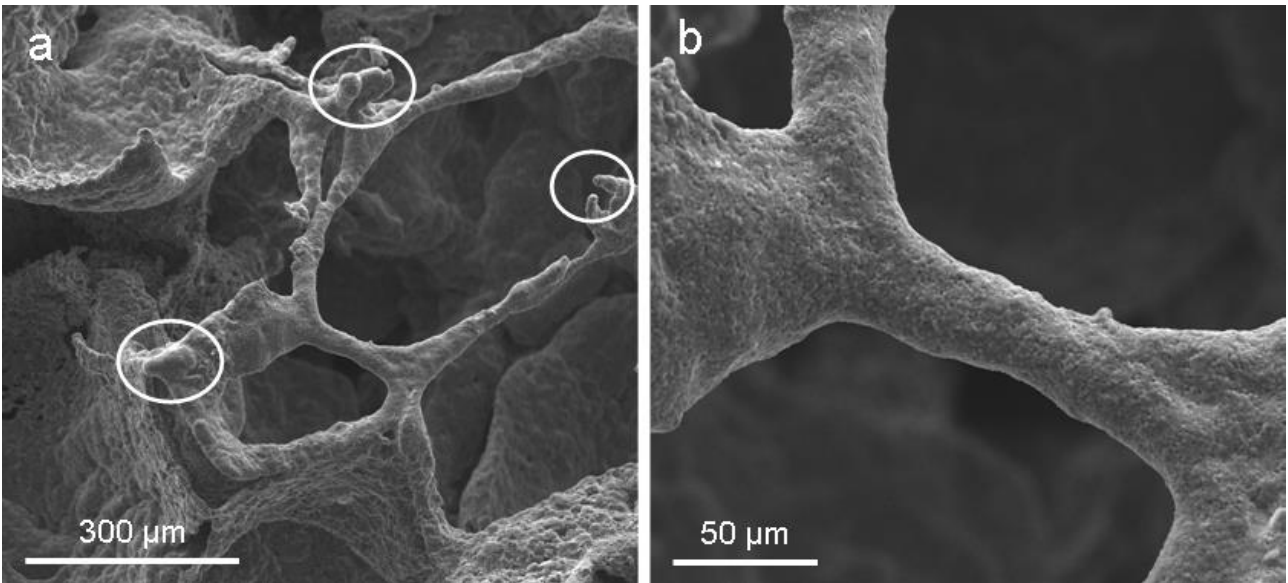


**Figure 11.** GC-CEL2 scaffolds architecture: (a) polished cross-section (magnification 40 $\times$ ) and (b) 3-D strut network (magnification 200 $\times$ )

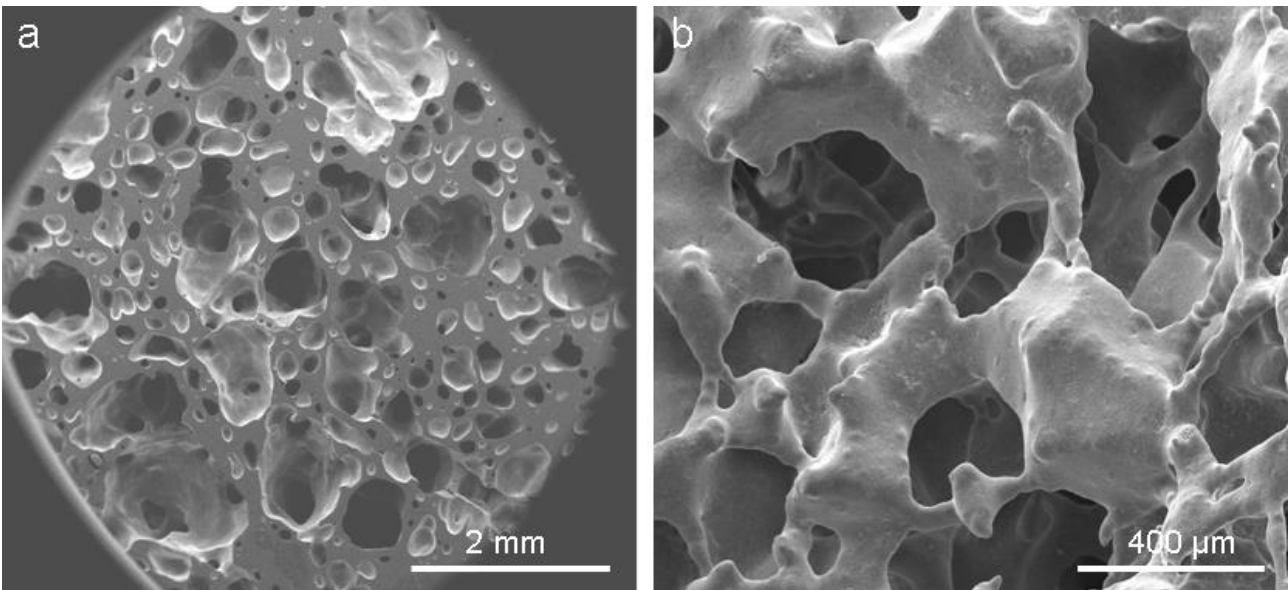


**Figure 12.** Pores size distribution resulting from image analysis on polished GC-BG32-1180, GC-BG5-1100 and GC-CEL2 scaffolds cross-sections.

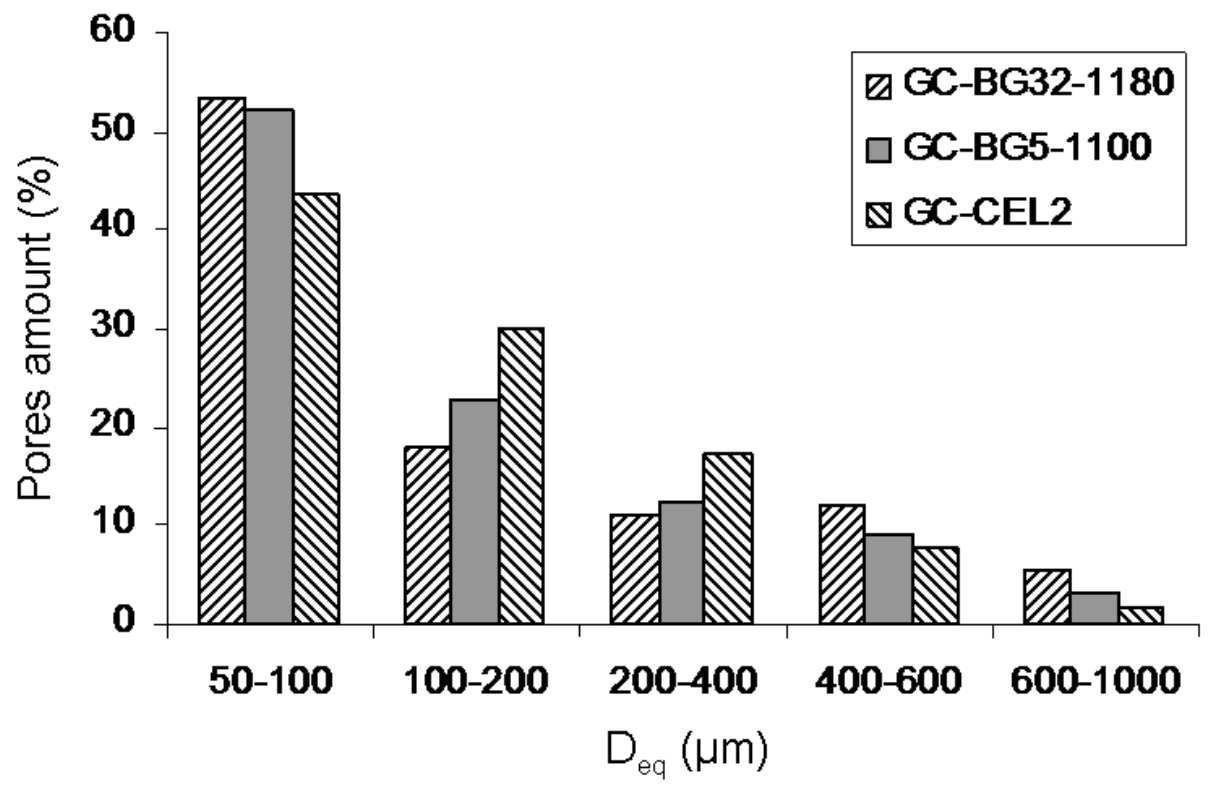


**Figure 13.** Comparison of typical stress-strain curves of GC-BG32-1180, GC-BG5-1100 and GC-CEL2 scaffolds.

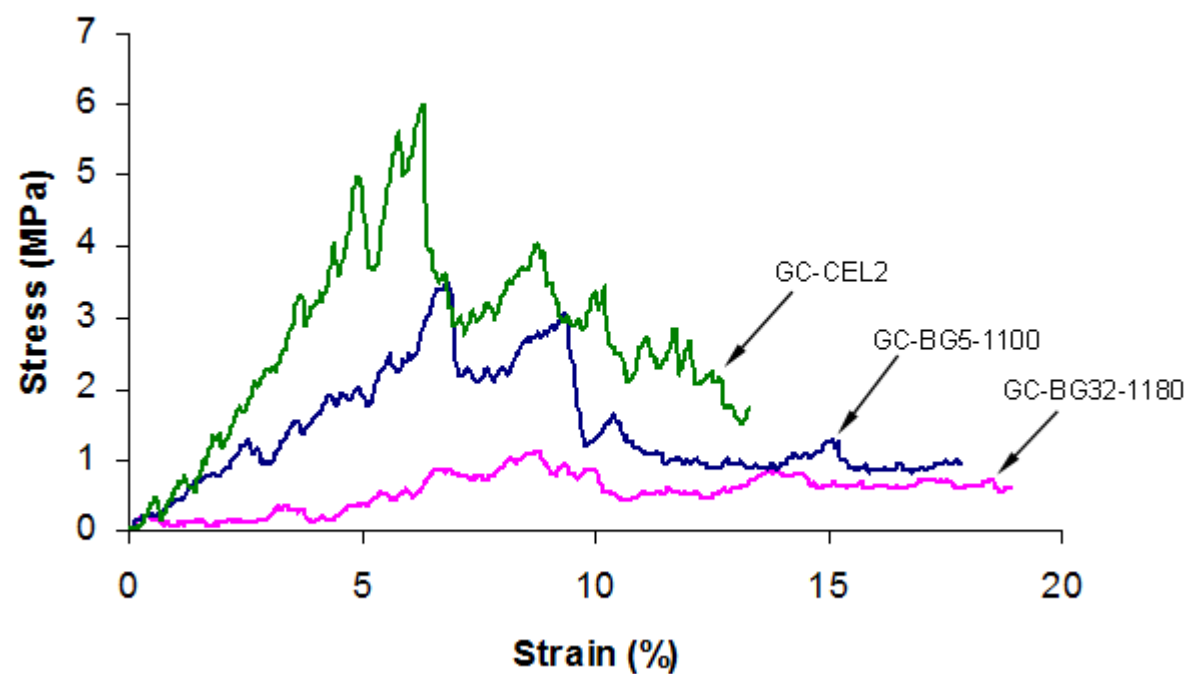




**Figure 14.** Relationship between porosity and compressive strength of the glass-derived scaffolds produced in this work: (a) linear and (b) quadratic model data fitting.

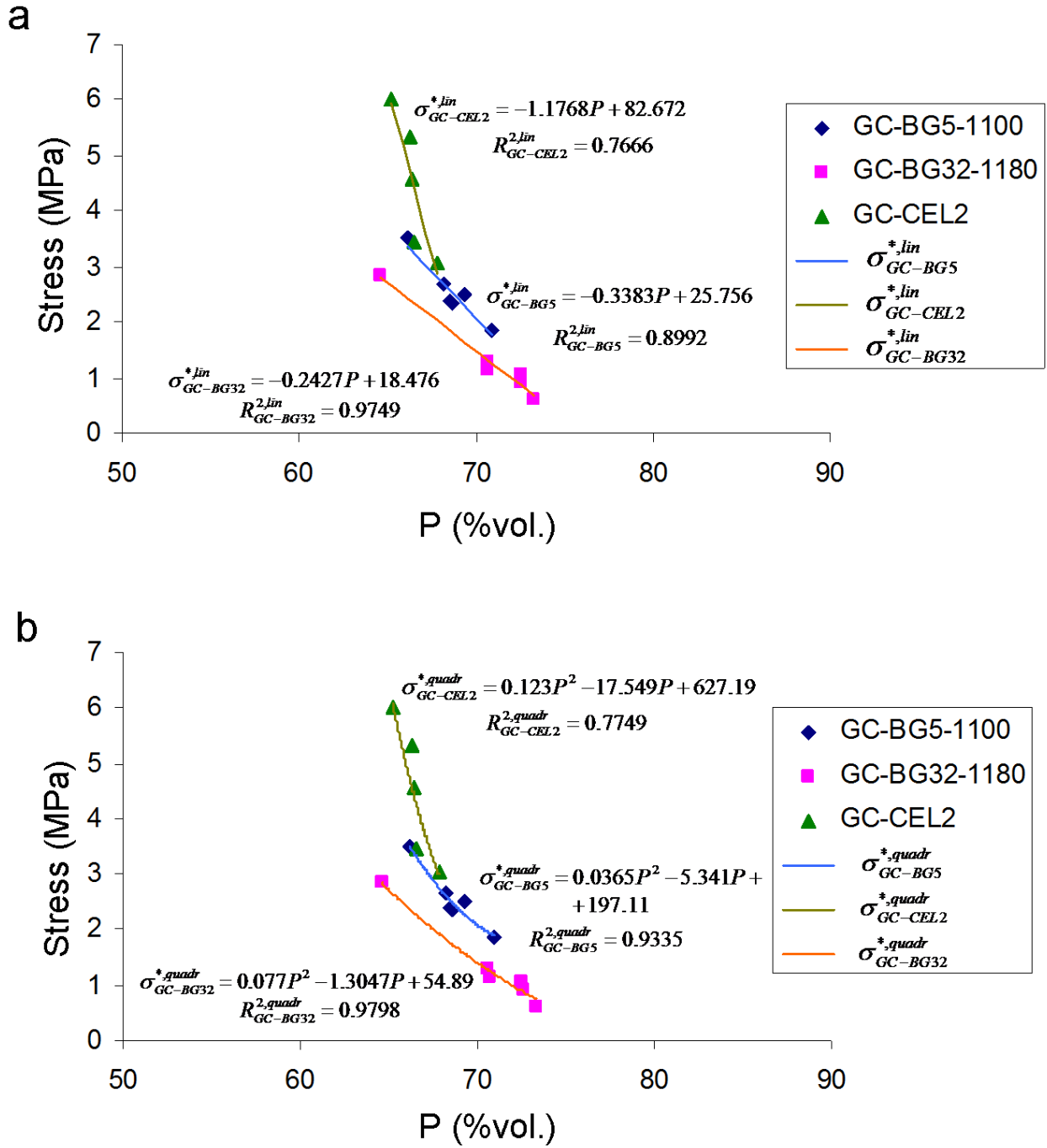


**Figure 15.** *In vitro* bioactivity of the scaffolds after soaking for 7 days in SBF: (a) surface of GC-BG32-1180 (magnification 5000×) and (b) corresponding EDS pattern; polished cross-sections of resin-embedded (c) GC-BG32-1180 scaffold (magnification 200×) and (d) GC-CEL2 scaffold (magnification 240×).

